UNIVERSITA' DEGLI STUDI DI PADOVA
Facoltà di Ingegneria
Dipartimento di Ingegneria Industriale

Corso di Laurea Magistrale in Ingegneria Aerospaziale

NUMERICAL INVESTIGATION INTO THE PERFORMANCE OF RECONFIGURABLE GASEOUS PLASMA ANTENNAS

Relatore

Ch.mo Prof. Daniele Pavarin

Correlatore

Ch.mo Dott. Davide Melazzi

Laureanda: Paola De Carlo

Matricola 1035441

Anno Accademico 20013 - 20014

to my uncle Gianni,
and my grandmas

Contents

Abstract

Gaseous plasma antennas are devices that rely on plasma discharges to radiate electromagnetic fields. Compared to metallic antennas, they can (i) be reconfigurable in radiation pattern, frequency, bandwidth and input impedance, (ii) be tuned electrically rather than mechanically on microseconds time scales, (iii) be *transparent* above the plasma frequency allowing array configuration with reduced co-site interference. So far, several analytical and numerical models have been developed, though they rely on simplified plasma response. In this work we exploited ADAMANT, a full-wave numerical tool based on a set of coupled surface and volume integral equations, to fill the aforementioned gap in the study of how plasma parameters affect the performance of plasma antennas.

Firstly, we simulated a *plasma dipole* and *plasma torus* for the radiated fields and input impedance. In this analysis, we considered the current distribution in the plasma volume only, thus focusing on the plasma behavior as a radiating medium. Results show that the antenna radiation pattern can be reconfigured by adjusting plasma density, and signal frequency. In the dipole case, we considered also the effect of gas type, and magneto-static field, which are negligible in high density case, i.e., $n_0 > 10^{18}$ m^{-3}. This holds true for the real part of the impedance for both configurations, that decreases as the plasma density rises in all the working conitions simulated.

Secondly, we considered a $\lambda/2$ plasma dipole, and we computed the radiated fields due to the current distributions in the plasma volume as on the metal surface. We evaluated the influence of the driving circuit geometry on the radiation pattern assessing its key role, and we compared the plasma dipole against a metallic one for gain and directivity, which turned out to be similar; the gain is lower for the plasma dipole, due to the power absorbed by the plasma. The dipole was used in a linear *plasma array* comprised of two dipoles with axle spacing of $\lambda/2$, filled with a cold, non-magnetized, collisional plasma, with a density $n_0 = 10^{19}$ m^{-3}. Dipoles were excited in phase and in phase opposition; gain and directivity for different signal frequencies resemble that of an array of metallic dipoles for the same working conditions.

We assessed that GPAs act similar to metal antennas when the plasma density is high enough (i.e. $n_0 \geq 10^{19}$ m^{-3}), but with the possibility to reconfigure the radiation pattern in both shape and intensity by varying (i) the plasma density, (ii) the working frequency, and (iii) the magneto-static field (if present), giving to plasma antenna some advantages over conventional antennas.

Abstract italiano

Le antenne al plasma gassose sono dispositivi che utilizzano una scarica di plasma per irradiare campi elettromagnetici. Rispetto alle antenne metalliche, esse presentano diversi vantaggi: (i) sono riconfigurabili dal punto di vista di pattern di radiazione, frequenza, ampiezza di banda e impedenza in ingresso, (ii) possono essere riconfigurate elettricamente anzichè meccanicamente in tempi dell'ordine del millisecondo, (iii) sono *trasparenti* al di sopra della frequenza di plasma, proprietà che permette il loro impiego in array con interferenze ridotte. Fino ad oggi sono stati sviluppati diversi modelli numerici, che si basano però su modelli di plasma semplificati. In questo lavoro di tesi, abbiamo colmato le lacune nello studio dell'influenza dei parametri di plasma sulle performance delle antenne al plasma tramite ADAMANT, un codice numerico full-wave basato su un sistema di equazioni integrali di volume e superficie.

Innanzitutto, abbiamo simulato un *dipolo al plasma* e una *spira al plasma* calcolandone i campi radiati e le impedenze in ingresso. In questa prima analisi, abbiamo considerato solo la distribuzione di corrente nel volume di plasa, essendoci concentrati sul comportamento del plasma quando utilizzato come mezzo per irradiare onde elettromagnetiche. I risultati mostrano che è possibile riconfigurare il diagramma di radiazione variando la densità di plasma e la frequenza del segnale. Nel caso del dipolo abbiamo analizzato anche l'influenza sulle performance del tipo di gas usato per la scarica di plasma e di un campo magnetostatico esterno, mostrando che l'effetto di questi parametri sul pattern di radiazione e sull'impedenza è trascurabile per alte densità ($n_0 > 10^{18}$ m^{-3}). Questo è confermato anche dalla parte reale dell'impedenza in input, che decresce all'aumentare della densità per tutte le configurazioni e le condizioni operative simulate. Successivamente, abbiamo considerato un dipolo al plasma lungo $\lambda/2$ e ne abbiamo calcolato i campi scatterati considerando il contributo delle distribuzioni di corrente sia nel plasma che sulle superfici metalliche. Prima abbiamo valutato l'effetto della geometria del circuito per la deposizione del segnale, scoprendo che ha un ruolo chiave nelle performance dell'antenna. Quindi abbiamo confrontato il guadagno e la direttività ottenuti per il dipolo al plasma con quelli ottenuti per un equivalente dipolo metallico. I risultati sono simili ma il dipolo al plasma ha un guadagno minore dovuto all'assorbimento di potenza da parte del plasma. Lo stesso dipolo al plasma è stato usato per un array composto da due dipoli distanti $\lambda/2$ l'uno dall'altro. I dipoli sono riempiti con un plasma freddo, collisionale e non magnetizzato avente densità $n_0 = 10^{19}$ m^{-3} e sono eccitati in fase ed in opposizione di fase. Il guadagno e la direttività ottenuti per differenti frequenze del segnale sono simili a quelli di un array di antenne metalliche nelle stesse condizioni operative.

Con questo lavoro di tesi è stato provato che le antenne al plasma gassose sono simili

alle antenne metalliche quando la densità di plasma è sufficientemente elevata ($n_0 \geq 10^{19}$ m^{-3}), ma con la possibilità di riconfigurare sia la forma del pattern di radiazione sia l'intensità del campo irradiato variando (i) la densità di plasma, (ii) la frequenza del segnale e (iii) l'intensità del campo magneto statico (se presente). Questa possibilità dà alle antenne al plasma gassose diversi vantaggi operativi rispetto alle antenne tradizionali.

List of Symbols

$\boldsymbol{E}$	electric field	$[V/m]$
$\boldsymbol{J}$	current density	$[A/m^2]$
I	current intensity	$[A]$
q	charge	$[C]$
f	frequency	$[Hz]$
ε_0	vacuum electric permittivity	$[F/m]$
μ_0	vacuum magnetic permeability	$[H/m]$
c	speed of light	$[m/s]$
n_0	plasma density	$[m^{-3}]$
λ_0	wavelength	$[m]$
$\boldsymbol{D}$	electric flux density	$[C/m^2]$
$\boldsymbol{B_0}$	magneto-static field	$[T]$
$\boldsymbol{G}$	Green's function	
σ	charge sign	
Z_0	free space impedance	$[\Omega]$
m	mass	$[Kg]$
ω	angular frequency	$[rad/s]$
k_0	free space propagation constant	$[rad/m]$

List of Acronyms

EM	ElectroMagnetic
GPA	Gaseous Plasma Antenna
RF	Radio Frequency
CW	Continuous Wave
AM	Amplitude Modulation
FM	Frequency Modulation
RCS	Radar Cross Section
SPA	Smart Plasma Antenna
FDTD	Finite-Difference Time-Domain
HF	High Frequency
SHF	Super High Frequency
PDP	Plasma Display Panel
VEP	Volume Equivalence Principle
SEP	Surface Equivalence Principle
MoM	Method of Moments
PEC	Perfect Electric Conductor
RWG	Rao-Wilton-Glisson
SWG	Schaubert-Wilton-Glisson

List of Figures

Chapter 1

Introduction

GPAs are devices that rely on a partially or fully ionized gas to radiate EM waves [1]. The antenna consists of an insulating tube filled with low pressure gas, ionized by applying RF power. A metal sleeve is wrapped all around to the tube to apply the communication signal. The plasma is actually powered by two different frequencies simultaneously: an excitation frequency to drive the plasma discharge and a working frequency to apply the signal so that it might be used for either transmission (both frequencies switched on) or reception (only the driving frequency switched on) [2]. Plasma antenna relies on the property of plasma to behave frequency-dependently when an EM wave impinge on a plasma volume. If the EM wave has frequency higher then the plasma frequency, it passes through the plasma without attenuation. On the contrary, if the incident EM wave frequency is lower than the plasma frequency, the plasma behaves as a metal conductor. Thanks to this property, a plasma column can be used to radiate EM waves with frequency below the plasma frequency. Although the idea is not new, in the last decade there has been a resurgence of interest in the use of plasma as antenna radiating element, and several experiments were conducted using discharge tubes to radiate EM waves, devices referred to as GPAs [3] , [4]. This interest is due to a number of potential advantages of GPAs over conventional metallic antennas, as they can be designed to be more reconfigurable than traditional metallic antennas [3] - [5]. Initial studies have concluded that the performance of a plasma antenna is equal to a copper wire antenna in every respect [5], [6], and they can be used for any transmission and/or modulation technique: CW, phase modulation, impulse, AM, FM, chirp, spread spectrum or other digital techniques. The same is true as to its value as a receive antenna.

1.1 Plasma antennas versus conventional antennas

In Fig. 1.1(a), and in Fig. 1.1(b) are respectively pictured a schematic of a plasma antenna, and a basic early GPA.

GPAs have potential advantages over conventional metallic antennas [5], namely:

1. they are reconfigurable with respect to their input impedance, radiation pattern, working frequency and bandwidth;

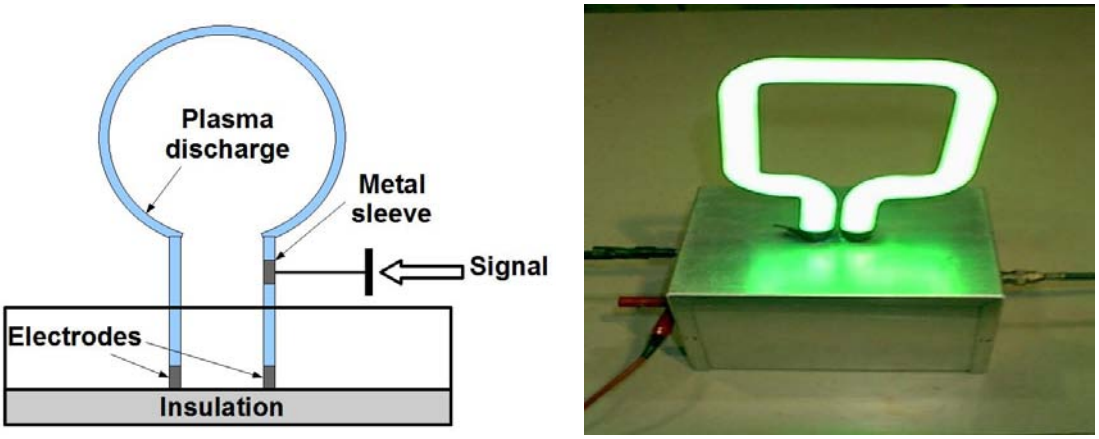

(a) (b)

Figure 1.1: (a) A schematic of a plasma antenna, and (b) a basic early plasma antenna.

2. they can be reconfigured electrically — rather than mechanically — on time scales the order of microseconds to milliseconds;

3. they reduce RCS, and have a lower thermal noise with respect to metal antennas;

4. they minimize signal degradation, being energized only while the communication takes place;

5. they are virtually *transparent* above the plasma frequency and become *invisible* once turned off [7].

Reconfiguration capabilities derive from accurately controlling plasma discharge parameters, such as: plasma density, applied magneto-static field (if any), and applied current. This parameters can be electrically adjusted by no mechanical means. Plasma antennas RCS reduction with respect to traditional antennas is possible thanks to the plasma discharge parameter reconfigurability. Metal antenna RCS depends on the geometric dimension of the device, while plasma antenna RCS is function of the plasma density. Reducing the working frequency, both metal and plasma antennas should rise in size to maintain geometric resonance and high efficiency. For a metal antenna, increasing in size means higher RCS value. This is not true for a plasma antenna. As the working frequency decreases, plasma density can be reduced, lessening the RCS. Moreover, there is a point in the RF spectrum at which the thermal noise of plasma antennas is equal to that of a metal antenna. At frequencies higher than this point, the plasma antenna noise decreases compared to a metal antenna. This point can be reduced in frequency by decreasing the plasma pressure. In addition, the collision rate in plasma antennas is much lower than in metal antennas thanks to the Ramsauer-Townsend effect. This contributes to reducing the plasma antenna thermal noise.

By reason of the plasma transparency, higher frequency plasma antennas can transmit and receive through lower frequency plasma antennas. Moreover, co-site interference are

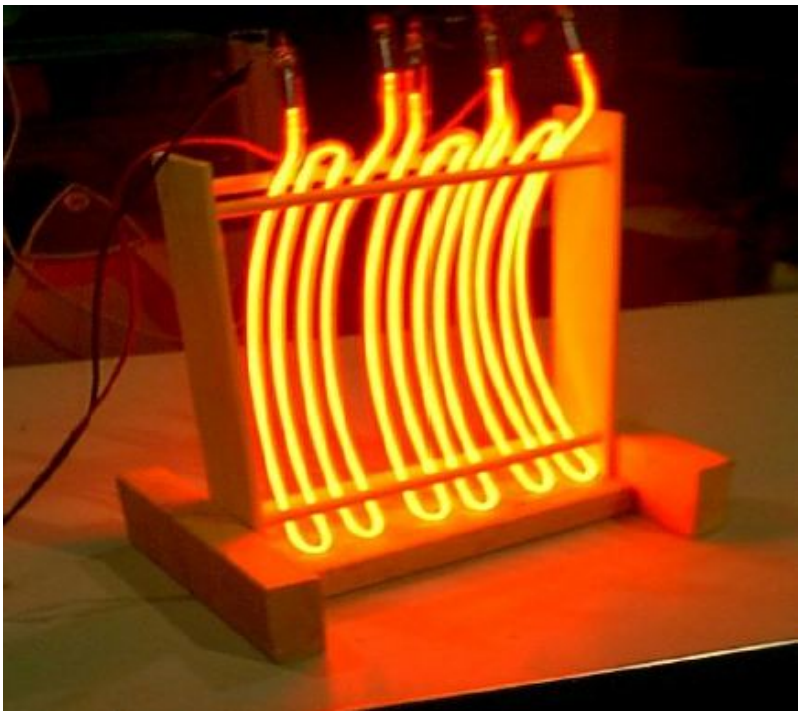

Figure 1.2: A plasma reflector prototype.

reduced or eliminated. This features allows plasma antenna to be used as frequency selective surface, also known as *plasma reflector* [8], [9], [10], and to be stacked into arrays [11]. A plasma reflector can be either a flat plasma discharge driven by a hollow cathod and a flat plate anode [12], or one or more banks of plasma tubes. A prototype of the latter is shown in Fig. 1.2. A plasma reflector can operate in reflective or refractive mode. In reflective mode the plasma frequency is higher then the working frequency, enabling the EM waves to be reflected off, while in refractive mode the plasma frequency is lower then the working frequency, so that the EM waves passes through the plasma. The reflector composed by an ensemble of plasma tubes can be flat or parabolic, enabling beam steering and focusing even if flat. EM waves reflecting off of a bank of plasma tubes are phase-shifted depending on plasma density in the tubes, and the same is valid for refracted EM waves [13]. This is similar to the effect of traditional phased array antenna, except for the phase shift controlling technology involved. Hence, it is possible to steer or focus the EM beam by independently varying the plasma density in tubes. For two dimensional steering or focus, two perpendicular banks of plasma tubes are needed. When used in refractive mode, the plasma reflector is often referred to as plasma lens and can be either divergent or convergent. A convergent plasma lens can focus EM waves to decrease beamwidth, increase directivity, and increase antenna range. Moreover, feed horns and receivers can be placed behind plasma antenna operating in refractive mode, eliminating the metal reflector problem of blind spots and feed losses.

Plasma-antenna arrays consist of either an ensemble of plasma antenna elements or one

metal antennas surrounded by plasma antennas, arranged to obtain the desired radiation pattern [14], [15], [16]. Besides the advantages already mentioned, from a theoretical point of view plasma-antenna arrays can:

1. be rapidly reconfigured without suffering from unused plasma elements, and without coupling unwanted power into nearby receivers;

2. be multi-band, each plasma antenna element working at a different frequency [5];

3. do beam-forming, and beam-steering by controlling each element plasma density, and switching them on or off [15], [17].

Plasma antenna arrays are referred to SPA, when smart signal processing algorithms are implemented. The SPAs feature all the aforementioned advantages of GPAs; additionally, they allow (i) identifying the direction of incoming signal, (ii) to track and locate the antenna beam on the mobile/target, (iii) to steer the beam to any direction of interest minimizing interferences [18].

The above features are listed and compared against metal antennas in Tab. 1.1.

	Plasma Antennas (GPAs, and SPAs)	**Metal Antennas**
Frequency Reconfigurability	High - Electrically Based on plasma parameters	Low - Mechanically
Radiation Pattern Reconfigurability	High - Elctrically Based on plasma parameters	Low
Beamwidth	From single lobe to multi lobe Plasma focusing and 360° steerable in mill/micro seconds	Low controllability Narrow lobe with huge dish Beam deformation
Bandwidth Reconfigurability	Narrow, Multiband, Broadband	Narrow
Thermal Noise	Reduced by a ~ 40 factor	Low
RCS	Low or complitely vanished	High
Co-site interference	~ 40 dB less sensitive to adjacent antennas	High
Power consumption	High to generate the plasma discharge	Only Ohmic losses

Table 1.1: Plasma antenna, and metal antenna features (data from [5], [19]).

1.2 Theoretical and experimental works

Up to now several analytical and numerical models have been developed to study plasma antennas, and to support experimental investigations. Starting from the global model developed for a plasma source sustained by a surface wave [20], [21], it has been demonstrated that:

1. the conductivity and its profile control the radiation pattern and the communication performance;

2. the length of the plasma column increases as the square root of the applied RF power;

3. the method used for coupling the transmission signal into the antenna plays a key role in antenna efficiency [2];

4. thermal noise due to random motion of the electrons, and noise in the vicinity of the ion plasma frequency are the most important contributions to possible noise sources [22].

In order to reproduce accurately the plasma response and to study how the plasma parameters affect the antenna efficiency and radiation pattern, a self-consistent kinetic model of the plasma antenna has been developed [23], [24]. FDTD method has been used to compute plasma antenna parameters [25], [26], [27], and its radiation characteristics when plasma density profiles, and the effect of external magnetization have been taken into account [26]. However, the aforementioned numerical models rely on simplified plasma models, which can afford limited control on the GPA behavior. Recently, a full-wave numerical tool named ADAMANT [28] has been used to investigate the influence of plasma parameters into the performance of plasma antennas.

In this work we used ADAMANT to analyze how plasma parameters (i.e. plasma density, magneto-static field, working frequency) affect the performance of GPAs of different shapes and filled with different gases.

1.3 Related works and patents

Although plasma antennas have only become practical in recent years, a patent for an antenna using the concept was granted to J. Hettinger in 1919 [29]; since then theoretical and experimental investigations led to several patents. Among them, it is worth mentioning US patents [30], [31] that are concerned with the reconfigurable properties of plasma antennas, whereas US patent [32] reported on using a coaxial plasma sheet to steer the beam of an inner plasma antenna radiating EM fields in the HF and SHF bands.

US patents [33], [34] are related to plasma antenna array; the former relies on a reconfigurable array of variable conductive elements for reflecting, filtering and steering EM radiation from an inner transmitting antenna in a wide range of frequencies, while the latter exploits PDP technology to realize a plurality of localized gas discharge areas, each gas area being selectively ionized by energizing means to form a reflector to incident radiation.

There is a semiconductor alternative to gaseous plasma antenna, currently under development by Plasma Antennas LTD [35]. It is a solid-state electronically steerable antenna that can be generated from a sheet of semiconductor material by forming a pattern of localized plasma regions in the sheet, either by injecting carriers into, or by generating carriers in, selected regions. They are essentially a cluster of thousands of diodes on a silicon chip that produces a tiny dense cloud of electrons when charged. This cloud can reflect high-frequency waves like mirrors do, focusing the beams by selectively activating particular diodes. Plasma Antennas LTD is currently developing this approach to build a controllable plasma reflector for small cell backhaul, midrange WiGig access point, and intelligent transportation systems; a technology demonstrator has been built in the $7 - 9$ GHz frequency band. It is worth noticing that this alternative works in the high frequency band, whereas, theoretically, there would be no upper or lower bound to GPAs in the RF spectrum.

Chapter 2

ADAMANT numerical code

In this chapter, we give a brief overview of ADAMANT numerical code, explaining then how is used. ADAMANT is a full-wave numerical tool that relies on a set of coupled surface and volume integral equations; these governing equations are numerically solved through the MoM in the form of Galerkin. The code solves for the surface electric current density on the metal surface driving the signal, and the volume polarization current in the plasma volume. This approach allows to analyze the fields radiated by the current density distribution in the plasma volume, and on the metal surface, enabling the accurate evaluation of GPA performance in terms of radiation pattern, and input impedance as a function of plasma discharge parameters.

2.1 Problem formulation

A realistic EM model of a GPA should include (i) the plasma volume(s) V_P, and (ii) the metallic part(s) S_A, which are immersed in a background medium. We formulate the EM problem by applying both the volume and the surface equivalence principle. The VEP requires introducing a set of polarization currents

$$\begin{aligned} \boldsymbol{J}_{Pk}(\boldsymbol{r}) &= j\omega\left[\overline{\boldsymbol{I}} - \overline{\varepsilon}_{rk}^{(-1)}(\boldsymbol{r})\right] \cdot \boldsymbol{D}_{Pk}(\boldsymbol{r}) \\ &= j\omega\overline{\boldsymbol{\alpha}}_k(\boldsymbol{r}) \cdot \boldsymbol{D}_{Pk}(\boldsymbol{r}), \end{aligned} \tag{2.1}$$

for $k = 1, \ldots, N_P$, with N_P being the number of indipendent plasma columns that forms the GPA and $\boldsymbol{D}_{Pk}$ the total displacement vector within the kth plasma region. The tensors $\overline{\varepsilon}_{rk}$ denote the plasma permittivity tensors relative to free space in the kth plasma region.

In GPAs, the plasma is cold, weakly collisional, and magnetized. Thus, in a system of Cartesian coordinates with $\boldsymbol{B_0} = B_0\hat{\boldsymbol{z}}$, the dyadics $\overline{\varepsilon}_{rk}$ take the form

$$\overline{\varepsilon}_{rk} = \begin{bmatrix} S_k & jD_k & 0 \\ -jD_k & S_k & 0 \\ 0 & 0 & P_k \end{bmatrix}, \tag{2.2}$$

with the Stix parameters defined as follow:

$$S = 1 - \sum_{\xi} \frac{\omega_{p\xi}^2(\omega - j\nu_\xi)}{\omega\left[(\omega - j\nu_\xi)^2 - \omega_{c\xi}^2\right]} \tag{2.3a}$$

$$D = \sum_{\xi} \frac{\sigma_\xi \omega_{c\xi}}{\omega} \frac{\omega_{p\xi}^2}{\left[(\omega - j\nu_\xi)^2 - \omega_{c\xi}^2\right]} \tag{2.3b}$$

$$P = 1 - \sum_{\xi} \frac{\omega_{p\xi}^2}{\omega\left(\omega - j\nu_\xi\right)} \tag{2.3c}$$

where $\omega_{p\xi} \equiv \left(n_\xi q_\xi^2/\varepsilon_0 m_\xi\right)^{1/2}$ is the plasma frequency, σ_ξ indicates the particle charge sign, $\omega_{c\xi} \equiv \sigma_\xi q_\xi B_0/m_\xi$ is the gyrofrequncy, and ν_ξ is the collision frequency. The subscript ξ refers to the index of the plasma species.

We apply the SEP to the metallic parts. We assume all the metallic parts as PEC, and we model the metallic sleeve excitation by means of the so-called *voltage gap*, which requires setting the voltage V_G at the circuit port and computing the current I_A therein [36], [37], [38]. It is worth recalling that the voltage gap model can be applied as long as the actual antenna port is small as compared to (i) the operational wavelength in the background medium, and (ii) the antenna size. As a result of SEP application, the metallic parts are replaced with an unknown electric surface density $\boldsymbol{J}_A$.

The currents $\boldsymbol{J}_A$ and $\boldsymbol{J}_P$ constitute the two unknowns to be determined.

2.2 Governing equations

We apply the boundary conditions on the metal surface S_A, which states that the tangent component of the electric field upon a PEC surface is zero, and we express the total electric field in the N_P plasma regions as

$$\boldsymbol{E}_P(\boldsymbol{r}) = \boldsymbol{E}_{PA}^S(\boldsymbol{r}) + \boldsymbol{E}_{PP}^S(\boldsymbol{r}), \qquad \boldsymbol{r} \in V_P \tag{2.4}$$

where $\boldsymbol{E}_{PA}^S$ $\left(\boldsymbol{E}_{PP}^S\right)$ represents the secondary electric field produced by $\boldsymbol{J}_A$ $(\boldsymbol{J}_P)$ within V_P. By enforcing the boundary condition for S_A, and Eq. 2.4 we arrive at a set of coupled surface and volume integral equations

$$\begin{aligned} \boldsymbol{E}_A^i(\boldsymbol{r}) + \omega^2\mu_0\overline{\boldsymbol{G}}(\boldsymbol{r}) \overset{*}{\cdot} \left[\sum_{k=1}^{N_P} \overline{\boldsymbol{\alpha}}_k(\boldsymbol{r}) \cdot \boldsymbol{D}_{Pk}(\boldsymbol{r})\right] \\ -\boldsymbol{j}\omega\mu_0\overline{\boldsymbol{G}}(\boldsymbol{r}) \overset{*}{\cdot} \boldsymbol{J}_A(\boldsymbol{r})\Big|_{tan} = 0, \qquad \boldsymbol{r} \in S_A, \end{aligned} \tag{2.5}$$

$$\begin{aligned} \overline{\varepsilon}_r^{-1} \cdot \boldsymbol{D}_{Pk}(\boldsymbol{r}) = -\boldsymbol{j}\omega\varepsilon_0\mu_0\overline{\boldsymbol{G}}(\boldsymbol{r}) \overset{*}{\cdot} \boldsymbol{J}_A(\boldsymbol{r}) \\ + k_0^2\overline{\boldsymbol{G}}(\boldsymbol{r}) \overset{*}{\cdot} \left[\sum_{l=1}^{N_P} \overline{\boldsymbol{\alpha}}_l(\boldsymbol{r}) \cdot \boldsymbol{D}_{Pl}(\boldsymbol{r})\right], \qquad \boldsymbol{r} \in V_{Pk}, \end{aligned} \tag{2.6}$$

where $\boldsymbol{E}_A^i$ is the impressed electric field at the metal surface port, $\overline{\boldsymbol{G}}(\boldsymbol{r})$ is the dyadic Green's function in free space, and '$\overset{*}{\cdot}$' denotes 3D spatial convolution and scalar product.

2.3 Numerical solution

We numerically solve the system of Eqs. 2.5, 2.6 by means of the MoM in the form of Galerkin. To this purpose, we model S_A with a 3D triangular-faceted mesh, and V_P with a tetrahedral mesh. We associate surface and volume div-conforming vector linear element $\boldsymbol{f}(\boldsymbol{r})$ and $\boldsymbol{v}(\boldsymbol{r})$ respectively with the inner edges of the triangular mesh, and with all facets of the tetrahedral mesh (see Appendix A, B), in order to expand the unknowns as follow:

$$\boldsymbol{J}_A(\boldsymbol{r}) \approx \sum_{n=1}^{N_A} \boldsymbol{f}_n(\boldsymbol{r})\, I_n, \qquad \boldsymbol{r} \in S_A \tag{2.7a}$$

$$\boldsymbol{D}_P(\boldsymbol{r}) \approx \sum_{p=1}^{N_P} \boldsymbol{v}_p(\boldsymbol{r})\, D_p, \qquad \boldsymbol{r} \in V_P \tag{2.7b}$$

Substituting Eqs. 2.7(a),(b) into Eqs. 2.5, 2.6, and projecting them respectively onto $\boldsymbol{f}_m$, $m = 1, \ldots, N_A$, and onto $\boldsymbol{v}_q$, $q = 1, \ldots, N_P$, we obtain the final algebraic system of rank $N_A + N_P$. In matrix form, it reads

$$\begin{bmatrix} [Z_{AA}] & [Z_{AP}] \\ [Z_{AP}] & [Z_{PP}] \end{bmatrix} \begin{bmatrix} Z_0\,[J_A] \\ [D_P]\,/\varepsilon_0 \end{bmatrix} = - \begin{bmatrix} [V_G] \\ [0] \end{bmatrix} \tag{2.8}$$

where Z_0 and ε_0 have been factored out and paired with the vectors of unknown coefficients to improve the conditioning of the matrix. With this positions, $Z_0\,[J_A]$ and $[D_P]\,/\varepsilon_0$ carry the physical dimensions of an electric field. The column vectors $[J_A]$ and $[D_P]$ contain the coefficients of $\boldsymbol{J}_A$ and $\boldsymbol{J}_P$ respectively. The entries of the excitation vector $[V_G]$ and of the four blocks in which the system matrix is naturally partioned are detailed in Appendix C.

2.4 ADAMANT user guide

In this section we give some baseline to use ADAMANT. We distinguished three phases in running ADAMANT, namely preprocessing, numerical solution, and postprocessing. We describe the operational process to follow in each phase in order to correctly run a simulation.

2.4.1 Preprocessing

We draw the geometries through GMSH [39], a free finite element mesh generator. We first draw the plasma volume, and we mesh it in tetrahedral elements. In Figs. 2.1(a),(b) a plasma column mesh example is pictured. Fig. 2.1(b) shows a longitudinal section of the mesh emphasizing the tetrahedral discretization of the volume. The mesh size can be controlled setting the characteristic length of the tetrahedral element for each point drawn.

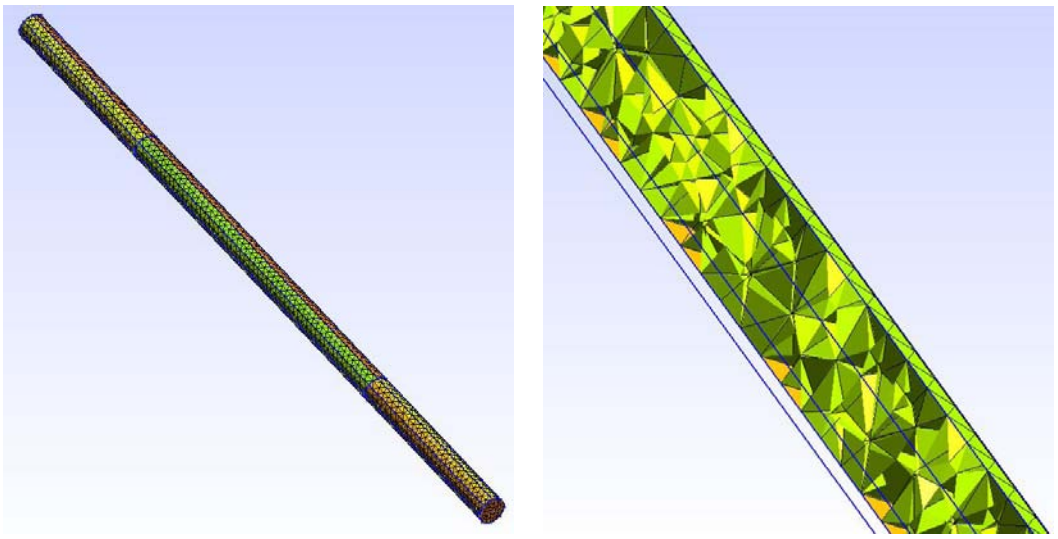

(a) (b)

Figure 2.1: (a) A plasma column mesh example, and (b) a particular of the longitudinal section.

The mesh is exported as **.msh* file to be processed by a customized mesh converter. The mesh converter generates a **.vie.msh* file. The latter is composed by four blocks:

1. The first block contains the vertex information. It is structured in five columns. The first reports the flag 1 identifying the *vertex block*, the second contains a number identifying each vertex, and the last three contain respectively the x, y, and z coordinates of each vertex;

2. The second block contains the triangle information. It is structured in six columns. The first reports flag 2 identifying the *triangle block*, the second contains a number identifying each triangle. The third, fourth, and fifth columns contain the numbers corresponding to the three vertexes composing the triangle, and the sixth reports the area of each triangle;

3. The third block contains the tetrahedron information. It is structured in twenty-two columns. The first reports the flag 3 identifying the *tetrahedron block*, the second contains a number identifying each tetrahedron, the next four columns report the identifying number of the four triangles that compose the tetrahedron, the next three columns report the barycenter coordinates, the tenth reports the tetrahedron volume. The last twelve columns contain the (x, y, z) components of the normals to each facet of the tetrahedron;

4. The fourth block contains the SWG information. It is structured in four columns. The first reports the flag 4 identifying the *SWG block*, the second contains a number identifying each function. The last two columns contains the identifying number of the two adjoining tetrahedrons on which the SWG is defined.

We draw the driving circuit, and we assign PEC material properties to the surface. We mesh the geometry in triangular elements, as shown in Fig. 2.2. We apply (with reference to *voltage gap* source type) the feeding by setting the port region composed by at least one couple of adjoining triangles. We assign to the two triangles of each couple the port, and ground material properties respectively. We can set up to four independent voltages, each a different port region.

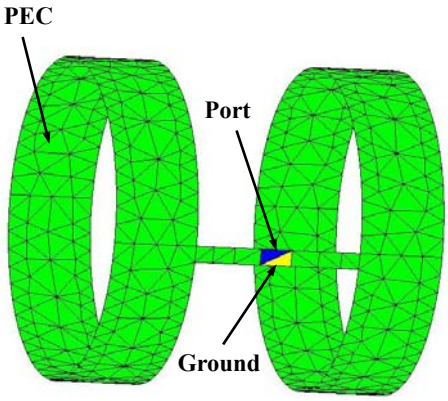

Figure 2.2: Driving circuit mesh example.

The mesh file has to be exported as **.inp* file and be processed by the appropriate mesh converter. The mesh converter generates a **.ant.msh* file, that is composed by three blocks:

1. The first contains the vertex information, and it is structured in five columns. The first reports the flag 1 identifying the *vertex block*, the second contains a number identifying each vertex, and the last three columns contain respectively the x, y, and z coordinates of each vertex;

2. The second block contains the triangle information. It is structured six columns. The first reports the flag 2 identifying the *triangle block*, the second contains a number identifying each triangle, the next three columns reports the number of the vertex composing each triangle, and the last column contains a flag identifying the material properties assigned to that triangle. The latter can be 1, -1, 11, 12, 13 or 14, indicating respectively the PEC, ground, port 1, port 2, port 3 or port 4 material properties.

3. The third block contains the RWG information, and it is structured in five columns. The first reports the flag 3 identifying the *RWG block*, the second contains a number identifying each function, the next two columns report the identifying numbers of the two adjoining triangles on which the RWG is defined.

2.4.2 Solution

ADAMANT needs four input files to run:

1. the **.vie.msh*;
2. the **.ant.msh*;
3. the *plasma.inp*;
4. the *adamant_data.inp*.

The *adamant_data.inp* contains the simulation parameters,

```
&geometry
      Sgeoname  = "ANTENNA MESH NAME"
      Vgeoname  = "VOLUME MESH NAME"
/
&settings
      sourcetype = "voltage_gap"
  dieltype = "plasma"
      ntheta = 180
      nphi = 180
  debugging = 0
/
&plasma
      gas = "Ar"
  species = 2
      Bzconf = 0
  Npress = 1.5d1
/
&param
      nports   = 1
/
&impedance
      Zref(1) = 50.0d0
      Zref(2) = 50.0d0
      Zref(3) = 50.0d0
      Zref(4) = 50.0d0
/
&feeding
      voltages(1) = (1.0d0,0.0d0)
      voltages(2) = (1.0d0,0.0d0)
      voltages(3) = (1.0d0,0.0d0)
      voltages(4) = (1.0d0,0.0d0)
/
```

```
&frequency
      fsim = 125d6
      dcellmax = 0.25
/
&Sintegration
      d_threshold = 3.0d0
      ord1(1:2) = 4 4
      ord2(1:2) = 4 4
      ord3(1:2) = 4 4
      ord4(1:2) = 4 4
/
&Vintegration
      sord1(1:2) = 1 3
      sord2(1:2) = 1 3
      sord3(1:2) = 3 4
      sord4(1:2) = 3 4
      vord1(1:2) = 1 3
      vord2(1:2) = 1 3
      vord3(1:2) = 3 4
      vord4(1:2) = 3 4
/
&background
      epr = (1.0d0,0.0d0)
      mur = (1.0d0,0.0d0)
/
```

The *adamant_data.inp* file is composed by ten blocks, each regarding some simulation parameters as follow:

geometry regards the geometry files, and it has to be completed with the mesh converted file names, for the surface and the volume, respectively;

settings is about simulation settings and it contains:

1. the source type, that can be *plain_wave* or *voltage_gap*. When the source type is set as *voltage_gap*, the code needs the ground and port material properties in the mesh converted file;
2. the dielectric type that can be *dielectric* or *plasma*. The code needs respectively a *dielectric.inp* or *plasma.inp* file to run.
3. the number of ϕ samplings, where the electric fields are evaluated in the far field region;
4. the number of θ samplings, where the electric fields are evaluated in the far field region;

plasma regards the plasma and it contains:

1. a gas flag, that is the element symbol, and can be:
   a) *Ar*,
   b) *N2*,
   c) *H2*,
   d) *He*,
   e) *Ne*;
2. the number of species;
3. the magneto-static field intensity $[T]$;
4. the neutral background pressure $[mTorr]$;

param reports the number of ports set in the excitation circuit geometry;

impedance is the reference impedance for each port $[\Omega]$; it contains four complex numbers, one for each port;

voltages is the voltage gap feeding each port $[V]$;

frequency is divided into two rows. The first reports the simulation working frequency $[Hz]$, while the second is a threshold parameter for the code;

Sintegration defines the surface numerical integration formulas;

Vintegration defines the volume numerical integration formulas;

background reports the electric permittivity ε $[F/m]$, and the magnetic permeability μ $[H/m]$ of the background medium.

The *plasma.inp* file contains the plasma parameters,

```
#species
      "electrons"
  -1.602176462d-19
  9.10938188d-31
  1.0d+19
  3.000000d+00
  1
#
#species
      "ions"
  +1.602176462d-19
  6.63367652e-26
  1.0d+19
  3.0000000d-02
  1
#
```

The *plasma.inp* file is structured in two blocks, one for each species. Each block is composed by six rows:

1. the name of the species considered in the block;
2. the charge $[C]$;
3. the mass $[Kg]$;
4. the density $[m^{-3}]$;
5. the temperature $[eV]$;
6. a flag representing the plasma collisionality, that can be either 1 if the plasma is collisional, or 0 if it is not.

2.4.3 Running ADAMANT

ADAMANT can be run by typing

```
> ./adamant
```

on the command line.

2.4.4 Postprocessing

ADAMANT generates four outputs files:

adamant_PEC_Ja.txt reports the current distributed onto the metal surface. It is composed by four columns. The first column reports the port number associated with that solution of the EM problem, the second is the RWG identifying number, and the last two indicate respectively the real, and imaginary part of the current for each function.

adamant_PEC_param.txt contains the real and imaginary parts of the admittance, impedance, S parameters for each port combination, and the input power in different blocks. Each block is composed by four columns, the first two reporting the ports associated with the solution, and the last two respectively the real and imaginary parts of the parameter considered. In the input power block, the first two columns report the value 0.

adamant_DIELECTRIC_D.txt reports the current distribution in the plasma volume. It is structured in four columns. The first column reports the port number associated with the solution of the EM problem, the second is the SWG identifying number, and the last two indicate respectively the real, and imaginary part of the current for each function.

Es_farzone.txt contains the electric far field intensity evaluated in the (θ, ϕ) coordinate point in the far field region.

Customized MATLAB scripts have been developed to load simulation output files and to produce plot in a suitable form. A first script was developed in order to:

1. load the *Es_farzone.txt* file;

2. find the absolute maximum value of the scattered field intensity, and the maximum for each of the principal planes;

3. transform the scattered field intensity from spherical coordinates (ρ, θ, ϕ) into Cartesian coordinates (x, y, z);

4. plot the solid radiation pattern normalized to the absolute maximum;

5. plot the radiation patterns onto the principal planes normalized to the maximum for each plane.

In Fig. 2.3 an example of a solid radiation pattern plot obtained with the script is given, while Figs. 2.4(a),(b),(c) show a the corresponding polar radiation patterns respectively on the xOz, yOz, and xOy planes.

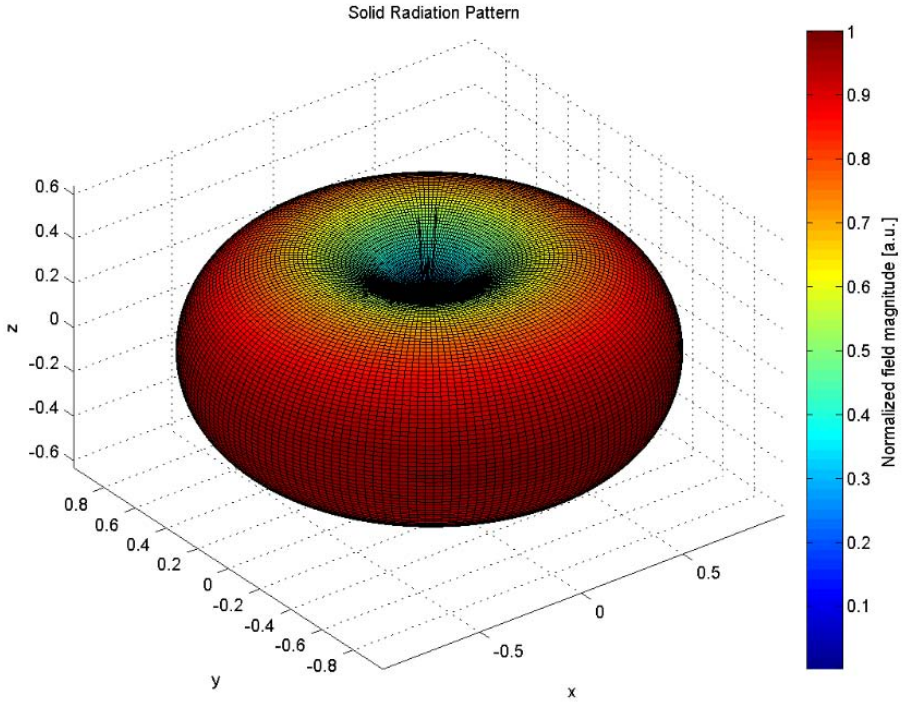

Figure 2.3: Example of script output: a solid radiation pattern of a dipole with the axes aligned with the $\hat{\boldsymbol{z}}$ direction.

A similar script was developed to compute the gain and the directivity, by means of a subroutine to load the input power from *adamant_PEC_param.txt* and to calculate the radiated power.

Another script was written to load the input impedance from *adamant_PEC_param.txt*, and to plot it as a function of a parameter given in input.

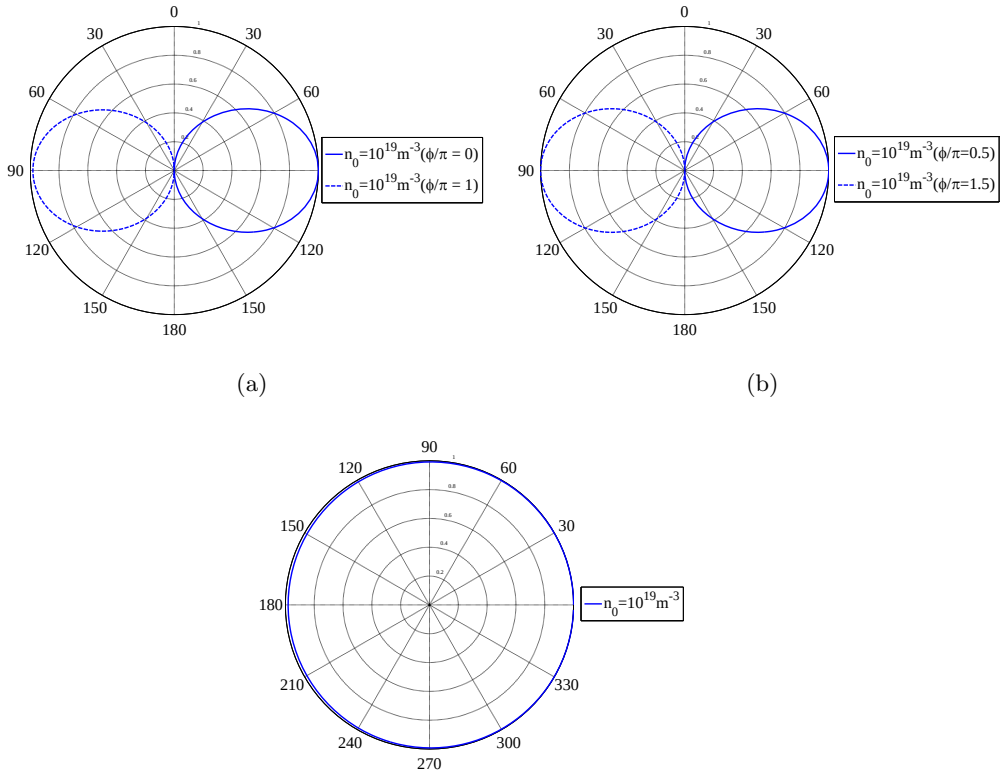

Figure 2.4: Example of normalized radiation pattern on (a) xOz, (b) yOz, and (c) xOy planes obtained with the customized Matlab script.

Chapter 3

Convergence analysis

The accuracy of the numerical results depends upon the number of RWG and SWG functions used to represent the current distributions on the driving circuit surface and in the plasma volume, respectively. However, the higher the number of functions, the longer is the simulation time; therefore, the number of functions to be used in the simulation is a trade off, and so a convergence analysis is necessary before doing any further investigation.

3.1 Driving parameters

We investigated the influence of the RWG, and SWG number in the numerical solution. To this purpose, we considered several meshes with different numbers of triangular and tetrahedral elements. We simulated each mesh for the radiation pattern and input impedance; finally, we compared them expecting to find an asymptotic behavior.

We find out that the main driving parameters in the RWG and SWG number assessment are: (i) the working frequency f_0, (ii) the geometry, (iii) the plasma discharge parameters. The most affecting parameters are the working frequency, and the geometry.

Since RWG and SWG are defined on triangular and tetrahedral elements (see Appendix A, B), the requirements on the number of RWGs and SWGs can be translated into requirements on the number of triangular and tetrahedral patches. As a rule of thumb:

1. at least 10 triangular (tetrahedral) mesh element for each λ_0;

2. the areas of the metal surface mesh triangles, and that of the tetrahedron facets in the plasma volume should be as similar as possible;

3.2 Cylindrical plasma discharge

We considered a cylindrical plasma discharge with the axis aligned along the $\hat{\boldsymbol{z}}$ direction, and driven by a metal sleeve wrapped around it. We assessed the number of RWGs, and SWGs to use for the numerical solution by simulating the cylinder with different RWG, and SWG numbers. To this purpose, we drawn three different meshes for the plasma volume, and three different meshes for the metal parts. The plasma volume meshes have

respectively ~ 12000, ~ 20000, and ~ 30000 SWGs, while the metal surface meshes have ~ 130, ~ 1000, and ~ 4000 RWGs.

We simulated the cylindrical plasma discharge on varying the SWG number but keeping constant the RWGs, and we computed the radiated fields, and the input impedances due to the contribution of the plasma current density in the plasma volume only. We then simulated it on varying the RWG number for a given number of SWGs, and we evaluated the radiation patterns, and the input impedance obtained considering the current distributions on the metal surface and in the plasma volume.

The radiation patterns obtained for a cylindrical plasma discharge with a plasma density $n_0 = 10^{16}$ m^{-3} on varying the SWG number for a given number of RWGs (~ 1000) are shown in Figs. 3.1(a),(b) on xOy plane and on yOz plane respectively, while the real and imaginary parts of the input impedance are respectively plotted in Figs. 3.2(a),(b) as functions of SWGs.

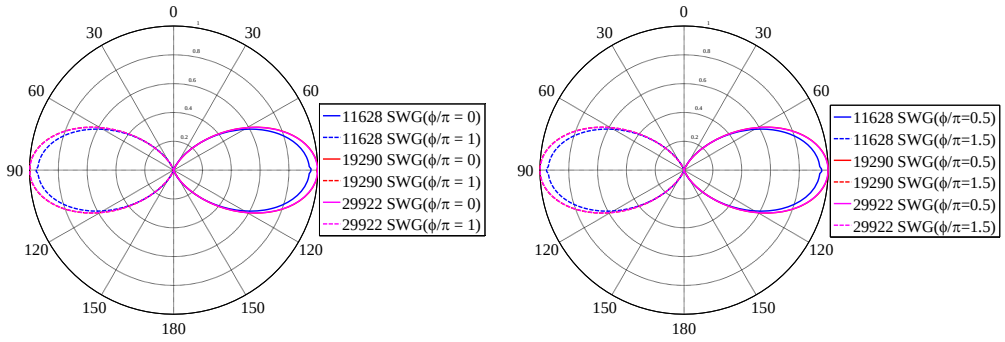

(a) (b)

Figure 3.1: Normalized radiation pattern on varying the SWG number for a given number of RWG (~ 1000) of the cylindrical plasma discharge for a uniform argon plasma driven at $f_0 = 125$ MHz, with a magneto-static field $B_0 = 0$ mT, and a plasma density $n_0 = 10^{16}$ m^{-3} on (a) xOz plane and (b) yOz plane.

As shown in Figs. 3.1(a),(b), the solution have an asymptotic behavior with respect to the SWG number, and the result obtained with ~ 20000 SWGs equals the results with ~ 30000 SWGs. The input impedance follows the same trend, and it rises as the SWG number does so, until ~ 2000 SWGs. The real part has the same value for ~ 20000, and ~ 30000 SWGs, confirming what already observed for the radiation pattern, while the imaginary part shows a small ($\sim 0.3\%$) variation.

The radiation patterns obtained for a cylindrical plasma discharge with a plasma density $n_0 = 10^{19}$ m^{-3} on varying the RWG number for a given number of SWGs (~ 10000) are shown in Figs. 3.3(a),(b) on xOy plane and on yOz plane respectively, while the real and imaginary parts of the input impedance are respectively plotted in Figs. 3.4(a),(b) as functions of RWGs.

As shown in Figs. 3.3(a),(b), changing the RWG number used for the simulation the radiation pattern is subjected to variations in both shape and intensity. It is worth to be

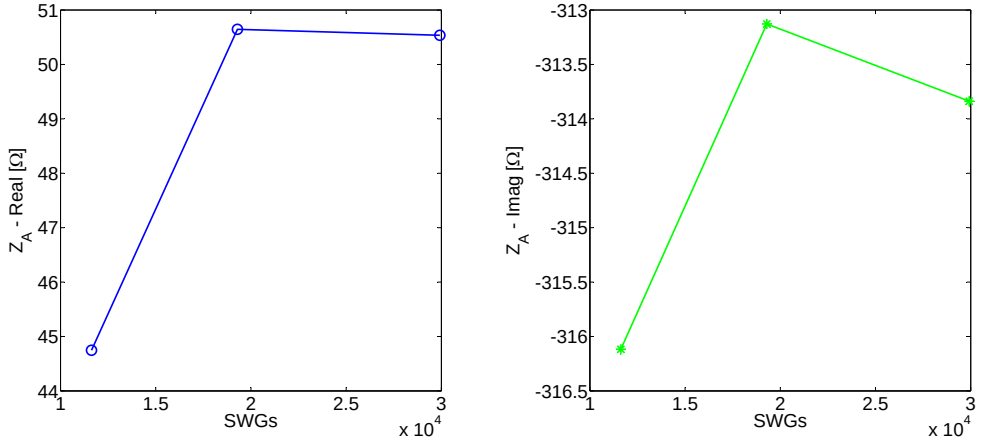

(a) (b)

Figure 3.2: (a) Real, and (b) imaginary parts of the input impedance as function of SWGs for a given number of RWG (~ 1000) of a cylindrical plasma discharge driven at $f_0 = 125\,\text{MHz}$, with a magneto-static field $B_0 = 0$ mT, and a plasma density $n_0 = 10^{16}$ m^{-3} .

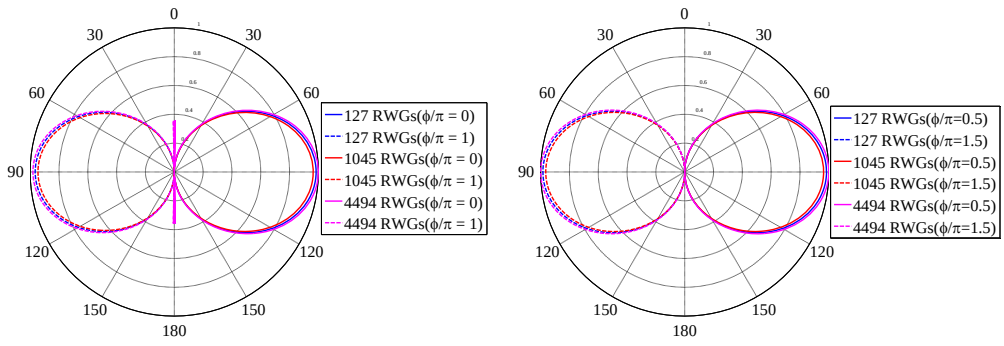

(a) (b)

Figure 3.3: Normalized radiation pattern on varying the RWG number for a given number of SWG (~ 10000) of the cylindrical plasma discharge for a uniform argon plasma driven at $f_0 = 2\,\text{GHz}$, with a magneto-static field $B_0 = 0$ mT, and a plasma density $n_0 = 10^{19}$ m^{-3} on (a) xOz plane and (b) yOz plane.

noted that for the driving circuit meshed with ~ 4500 RWGs, the radiation pattern on the xOz plane exhibits sidelobes that are not present in the other cases. This shape variation indicates that the characteristic dimensions of the triangular patches of the driving circuit mesh is small with respect to the tetrahedral facets of the plasma volume mesh, causing instability in the solution. This is confirmed by the real part of the input impedance trend,

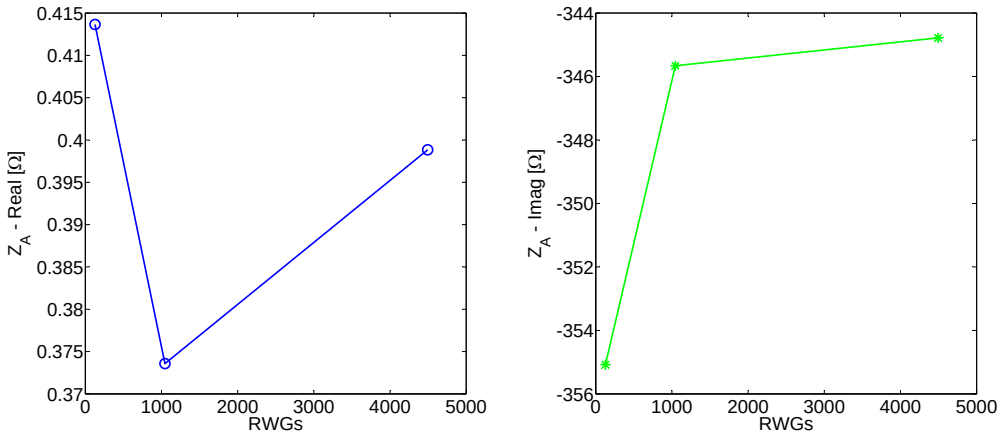

(a) (b)

Figure 3.4: (a) Real, and (b) imaginary parts of the imput impedance as function of RWGs for a given number of SWG ($\sim$ 10000) of a cylindrical plasma discharge driven at $f_0 = 2\,\mathrm{GHz}$, with $B_0 = 0$ mT, and a plasma density $n_0 = 10^{19}$ m^{-3} .

as shown in Fig. 3.4(a). The real part firstly decreases, and then rises of $\sim 5\%$ as the RWG number increases, and so the triangular patches on the metal surface mesh decreas in size with respect to the tetrahedral facets in the plasma volume. The imaginary part is less sensitive to the mesh unbalance, and shows again an asymptotic behavior.

3.3 Toroidal plasma discharge

We considered a toroidal plasma discharge driven by a metal sleeve placed at its bottom, and we assessed the RWG, and SWG numbers to use in the numerical simulation. We considered three different meshes for the plasma volume, having $\sim$ 11000, $\sim$ 20000, $\sim$ 31000 SWGs respectively, and we computed for each the scattered field due to the contribution of the current distribution in the plasma volume. We then analyze the influence of the RWG number considering three different meshes for the driving circuit, respectively with $\sim$ 200, $\sim$ 600, and $\sim$ 3000 RWGs, and computing the radiation pattern, and the input impedance for each taking into account the contribution of the current distributions in the plasma volume and on the metal surface.

The results of the sensitivity analysis on varying the SWG number for a given number of RWGs ($\sim$ 600) are shown in Figs. 3.5(a), (b) for a toroidal plasma discharge with a density $n_0 = 10^{19}$ m^{-3} on xOy plane and on yOz plane respectively. The corresponding real, and imaginary parts of the input impedance are plotted as functions of SWGs in Figs. 3.6(a),(b).

Figs. 3.5(a),(b) shows an asymptotic behavior with respect to the SWGs. The real part of the input impedance decreases as the number of SWG rises, while the imaginary part does not show a univocal trend. However, the variations are so small ($< 10\%$ for the

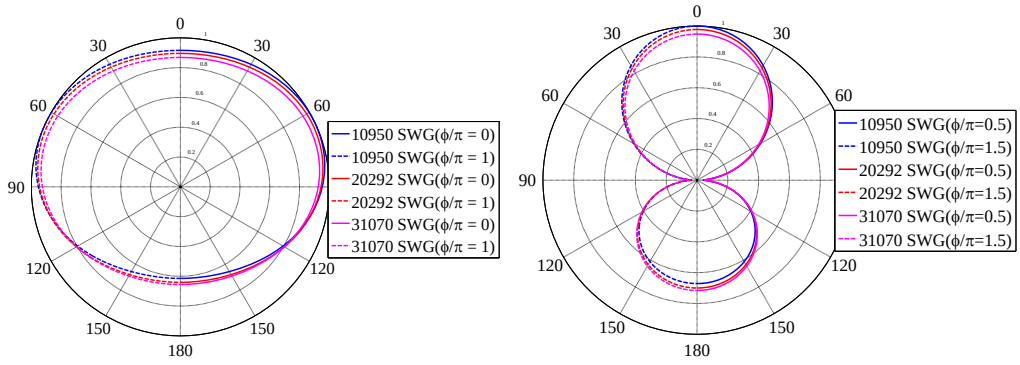

(a) (b)

Figure 3.5: Normalized radiation pattern on varying the SWG number for a given number of RWGs ($\sim$ 600) of the toroidal plasma discharge for a uniform argon plasma driven at $f_0 = 300\,\text{MHz}$, with a magneto-static field $B_0 = 0$ mT, and a plasma density $n_0 = 10^{19}$ m^{-3} on (a) xOz plane and (b) yOz plane.

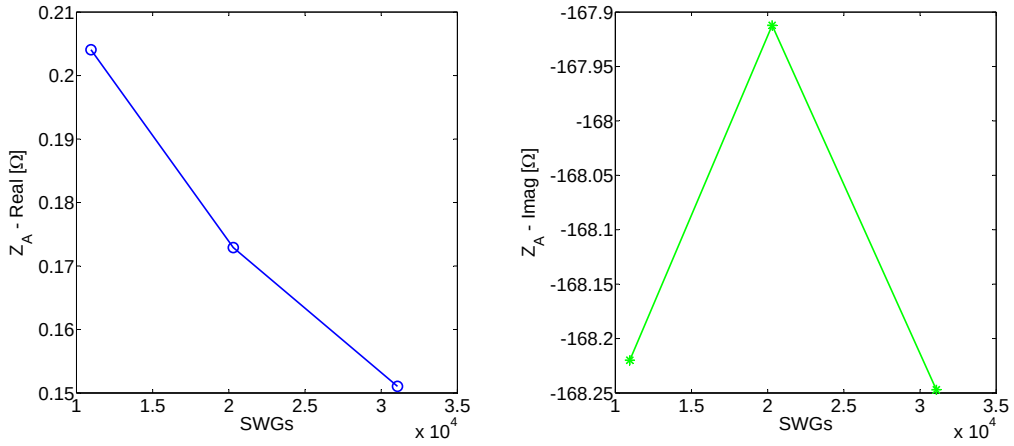

(a) (b)

Figure 3.6: (a) Real, and (b) imaginary parts of the imput impedance as function of SWGs for a given number of RWGs ($\sim$ 600) of a toroidal plasma discharge driven at $f_0 = 300\,\text{MHz}$, with a magneto-static field $B_0 = 0$ mT, and a plasma density $n_0 = 10^{19}$ m^{-3} .

real part, and $< 0.2\%$ for the imaginary part) that the input impedance parts can be both considered constants.

The results of the sensitivity analysis on varying the RWG number for a given number of SWGs ($\sim$ 10000) are shown in Figs. 3.7(a), (b) for a toroidal plasma discharge with a

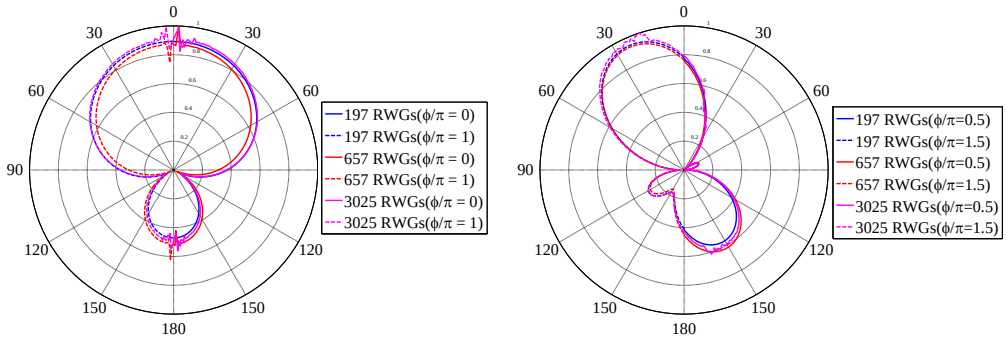

(a) (b)

Figure 3.7: Normalized radiation pattern on varying the RWG number for a given number of SWGs (~ 10000) of the toroidal plasma discharge for a uniform argon plasma driven at $f_0 = 300\,\text{MHz}$, with $B_0 = 0$ mT, and a plasma density $n_0 = 10^{19}$ m^{-3} on (a) xOz plane and (b) yOz plane.

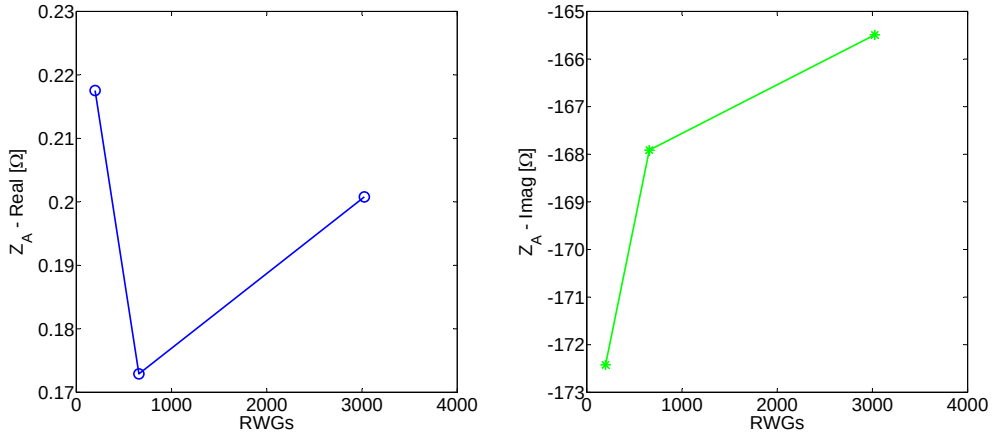

(a) (b)

Figure 3.8: (a) Real, and (b) imaginary parts of the imput impedance as function of SWGs for a given number of SWGs (~ 10000) of a toroidal plasma discharge driven at $f_0 = 300\,\text{MHz}$, with $B_0 = 0$ mT, and a plasma density $n_0 = 10^{19}$ m^{-3} .

density $n_0 = 10^{19}$ m^{-3} on xOy plane and on yOz plane respectively. The corresponding real, and imaginary parts of the input impedance are plotted as functions of RWGs in Figs. 3.8(a),(b).

The radiation patterns in Figs. 3.7(a),(b) show a variation with the RWG number in both shape, and intensity. Increasing RWG number can lead to numerical instabilities that destroy the solution accuracy, and caused spikes and irregularities in radiation pattern

shape, as can be seen in Fig. 3.7(a) for the driving circuits with ~ 600 and ~ 3000 RWGs, and in Fig. 3.7(b) for the case with ~ 3000 RWGs. The real part of the input impedance firstly decreases, and then increases as the RWG number rises, confirming what already observed for the radiation pattern shape, while the imaginary part tends to an asymptotic behavior.

3.4 Conclusions

Since the numerical result accuracy depends upon the number of RWGs, and SWGs used to simulate the driving circuit, and the plasma volume respectively, we performed a convergence analysis on a cylindrical and a toroidal plasma discharges. To this purpose, we simulated several meshes of the metal surface, and of the plasma volume for the radiation patters, and input impedance, and we compared the results obtained expecting to find an asymptotic behavior. We found out the the driving parameters in assessing the number of RWGs and SWGs are: (i) the working frequency, (ii) the geometry, and (iii) the plasma discharge parameters. As RWG and SWG are defined on triangular and tetrahedral elements, the requirements on the number of RWGs and SWGs can be translated into requirements on the mesh patches: (i) at least 10 triangular (tetrahedral) mesh element for each λ_0, (ii) the areas of the metal surface mesh triangles, and that of the tetrahedron facets in the plasma volume should be as similar as possible. For both configurations, we simulated three plasma volume meshes with different numbers of SWGs for a given number of RWGs, obtaining the radiation pattern and input impedance due to the plasma current distribution. Then we simulated three meshes of the driving circuit with different RWG numbers for a given volume mesh, and we evaluate the scattered fields due to the current distribution in the plasma volume, and on the metal surface.

The results obtained show that the solution has an asymptotic behavior with respect to the SWG, and RWG numbers. Moreover, increasing the RWG number can lead to numerical instabilities, which destroy the accuracy of the current distribution over the metal surface.

Chapter 4

Assessment on plasma parameters

We considered GPAs with different geometrical configurations, and we analyzed the influence of plasma discharge parameters on the radiated field in the far field region. First, we considered only the current density contribution $\boldsymbol{J}_P$, thus focusing on the behavior of plasma as conducting medium to radiate fields. We simulated a cylindrical, and a toroidal plasma discharge, and we evaluated the radiated fields, and input impedances. Radiated fields have been reported in polar radiation patterns. Numerical results show that the antenna radiation pattern can be reconfigured by adjusting the discharge parameters (i.e. density, magneto-static field, and working frequency).

4.1 Plasma dipole

We considered a cylindrical plasma column with the axis aligned along the $\hat{\boldsymbol{z}}$ direction. The cylinder is 120 cm long, and its radius is 1 cm. A 6 cm long metallic sleeve with a 1.4 cm radius is placed in the middle of the cylinder to drive the plasma discharge, as shown in Fig. 4.1. Hereinafter this configuration will be referred to as *plasma dipole*.

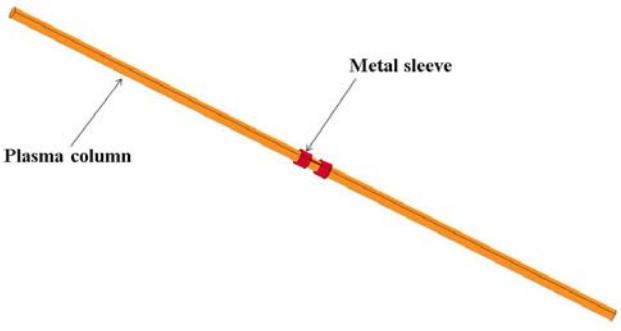

Figure 4.1: Plasma dipole configuration. The dipole axis is aligned with the $\hat{\boldsymbol{z}}$ direction.

In this analysis we considered radiated fields due to the $\boldsymbol{J}_P$ contribution only because

we wanted to analyze how the plasma parameters affect the plasma behavior as a conducting medium. We reported them on principal planes xOz, and yOz, and normalized to the maximum value for each plane. For the numerical solution we used ~ 20000 SWGs for the plasma volume, and ~ 1000 RWGs for the metal surface.

We considered a uniform argon plasma with an electron temperature of 3 eV, and a background neutral pressure of 15 mTorr. We computed the radiation pattern with: (i) the plasma density n_0 in the range $10^{16} - 10^{19}$ m^{-3}, (ii) the magneto-static field B_0 in the range $0 - 150$ mT, and (iii) the working frequency f_0 in the range $50 - 200$ MHz.

Figs. 4.2(a),(b) show the normalized radiation pattern of the plasma dipole for different values of n_0, with $B_0 = 0$ mT, and $f_0 = 125$ MHz, on the xOz and yOz respectively. The electric length of the plasma column is approximately $\lambda_0/2$.

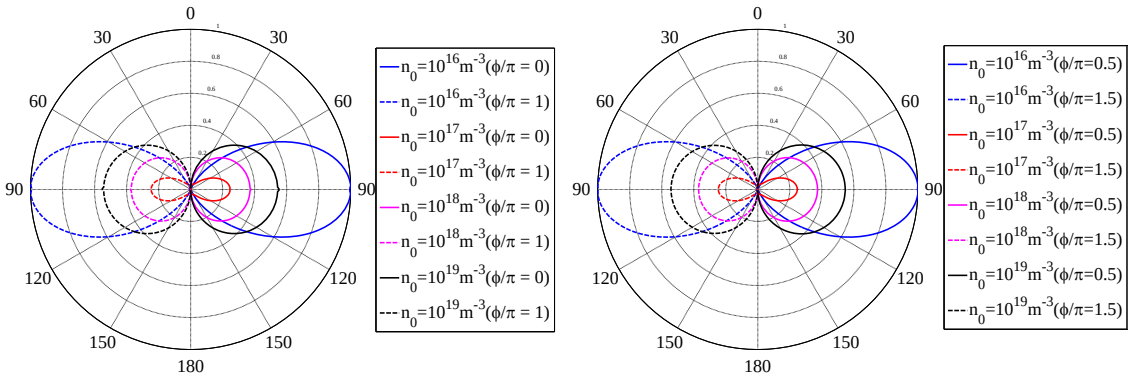

(a) (b)

Figure 4.2: Normalized radiation pattern of the plasma dipole for a uniform argon plasma driven at $f_0 = 125$ MHz, with a magneto-static field $B_0 = 0$ mT for different value of the plasma density n_0 on (a) xOz plane and (b) yOz plane.

Figs. 4.2(a),(b) show that the radiation pattern can be adjusted in terms of both intensity and shape by varying the plasma density in the column. As expected, the radiation pattern resembles that of a $\lambda_0/2$ metal dipole antenna. In addition, note that the radiation pattern on the plane xOz equals the pattern on the plane yOz. From now on only the result on the plane xOz will be shown.

Figs. 4.3(a),(b) show the radiation pattern for different values of the magneto-static field B_0, with $f_0 = 125$ MHz, for $n_0 = 10^{16}$ m^{-3}, and 10^{19} m^{-3} respectively.

Figs. 4.3(a),(b) show that the radiation pattern shape is insensitive to B_0 variation. The field intensity shows different behaviors depending to the plasma density: at plasma density $n_0 = 10^{17}$ m^{-3}, the field intensity reduces as the magneto-static field increases as shown in Fig. 4.3(a), while from Fig. 4.3(b) can be seen that the B_0 influence becomes negligible for higher values of n_0. The field magnitude reduction with the B_0 increasing it was noted also for densities lower than $< 10^{17}$ m^{-3}.

The results obtained for different values of the working frequency f_0, with $B_0 = 0$ mT, $n_0 = 10^{16}$ m^{-3} , and $n_0 = 10^{19}$ m^{-3} are shown respectively in Figs. 4.4(a),(b).

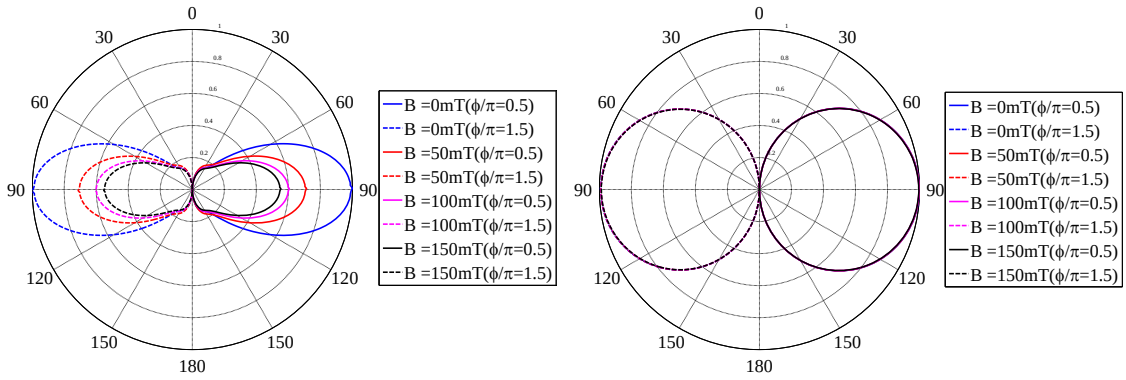

(a) (b)

Figure 4.3: Radiation pattern of an argon GPA dipole for different values of the magneto-static field B_0, with $f_0 = 125\,\text{MHz}$, (a) $n_0 = 10^{17}$ m^{-3}, and (b) $n_0 = 10^{19}$ m^{-3}.

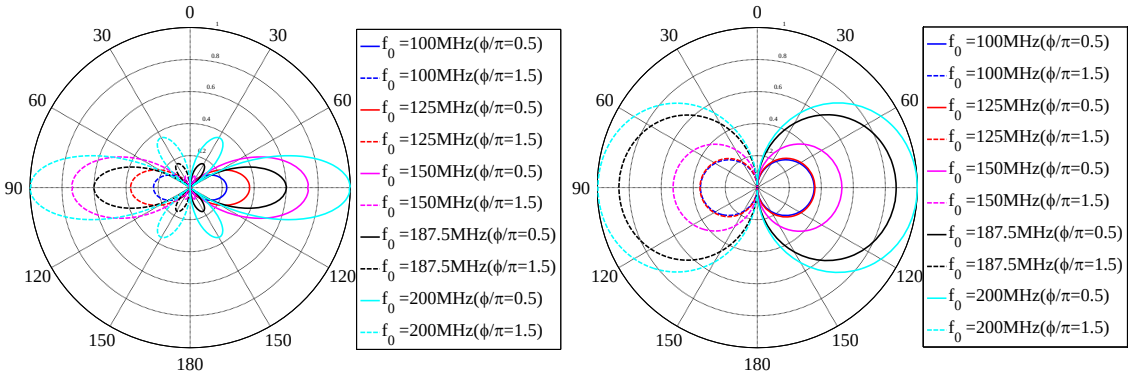

(a) (b)

Figure 4.4: Normalized radiation pattern of the plasma dipole for a uniform argon plasma for different value of the operating frequency f_0, with magneto-static field $B_0 = 0$ mT, plasma density (a) $n_0 = 10^{16}$ m^{-3}, and (b) $n_0 = 10^{19}$ m^{-3}.

The radiation patterns show no significant variations in shape for plasma density $n_0 \geq 10^{18}$ m^{-3}, while for lower values of density it exhibits sidelobes with higher intensity as the frequency increases. Adjusting the frequency it is possible to change the field intensity, obtaining a maximum value for the highest frequency tested.

Finally, we evaluated the performance with different gases. We considered a (i) neon, (ii) hydrogen, (iii) nitrogen, and (iv) helium plasma with an electron temperature of 3 eV, and a background neutral pressure of 15 mTorr.

The radiation pattern for each considered gas is pictured in Figs. 4.5(a),(b), for $B_0 = 0$ mT, and plasma density $n_0 = 10^{16}$ m^{-3}, and $n_0 = 10^{19}$ m^{-3} respectively. Figs. 4.5(a),(b)

shows that the radiation pattern do not depend in shape on the gas used for the plasma column. For $n_0 = 10^{16}$ m^{-3}, the field intensity exhibits a gas-dependent behavior. Increasing the density, the gap between the solutions gradually reduces. For a density $n_0 = 10^{19}$ m^{-3} the field intensity is insensitive to the gas used, as shown in Fig. 4.5(b).

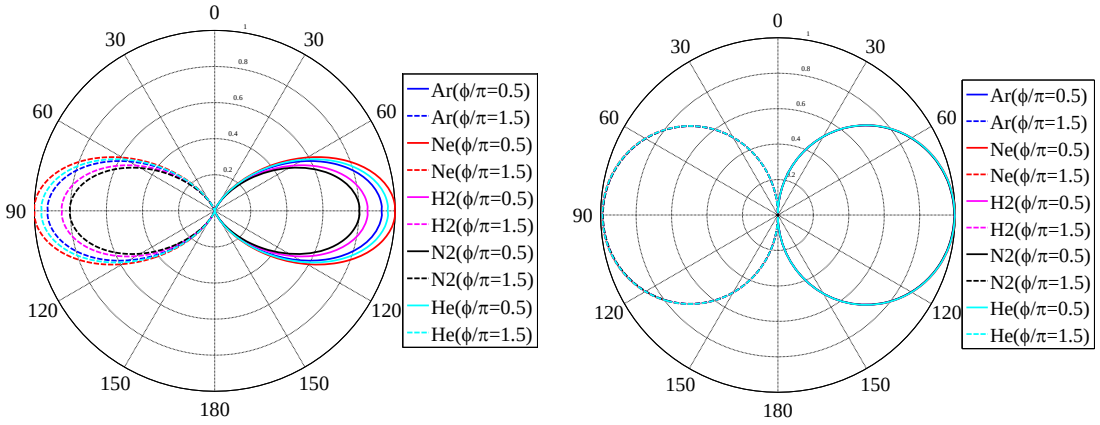

(a) (b)

Figure 4.5: Normalized radiation pattern of the plasma dipole for different gas with the working frequency $f_0 = 125$ MHz, a magneto-static field $B_0 = 0$ mT, a plasma density (a) $n_0 = 10^{16}$ m^{-3}, and (b) $n_0 = 10^{19}$ m^{-3}.

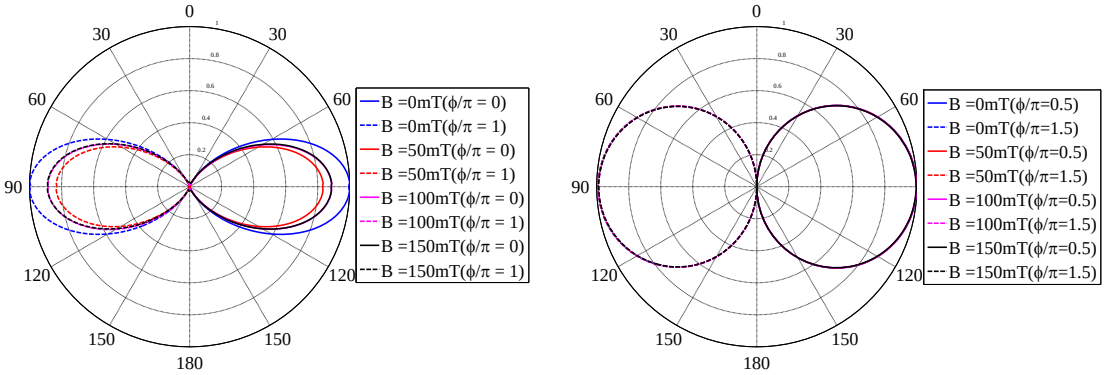

(a) (b)

Figure 4.6: Normalized radiation pattern of the nitrogen plasma dipole at different values of the magneto-static field with the working frequency $f_0 = 125$ MHz, and a plasma density (a) $n_0 = 10^{16}$ m^{-3}, and (b) $n_0 = 10^{19}$ m^{-3}.

In Figs. 4.6(a),(b) we plotted the radiation pattern of a uniform nitrogen plasma dipole

driven at $f_0 = 125$ MHz for different values of the magneto-static field, respectively for $n_0 = 10^{16}$ m^{-3}, and $n_0 = 10^{19}$ m^{-3}. As shown in Fig. 4.6(a), the radiation pattern for $n_0 = 10^{16}$ varies with B_0 in intensity but not in shape. The field magnitude has a maximum for $B_0 = 0$ mT, and a minimum for $B_0 = 50$ mT. Note that the patterns obtained for $B_0 = 100$ mT, and for $B_0 = 150$ mT are equal in both shape and intensity. At $n_0 = 10^{19}$ the radiation pattern is insensitive in both shape and magnitude, as can be seen from Fig. 4.6(b).

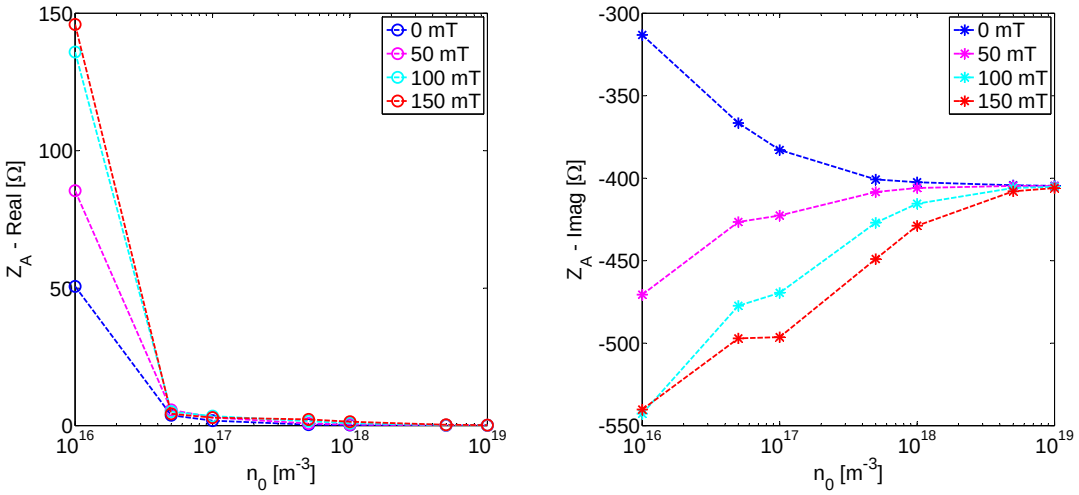

(a) (b)

Figure 4.7: (a) Real and (b) imaginary part of the input impedance as a function of n_0 for different values of B_0, and $f_0 = 125$ MHz.

As regards the GPA as a circuit element, we considered the real and imaginary parts of the input impedance. In Figs. 4.7(a),(b) we plotted the real and imaginary part of the input impedance as a function of the plasma density for different values of the magneto-static field, with $f_0 = 125$ MHz, while in Figs. 4.8(a),(b) we respectively plotted the real, and imaginary parts of the input impedance as function of n_0 for different gases, with $f_0 = 125$ MHz.

The results shown in Figs. 4.7(a),(b) indicate that the real part increases as B_0 does so for low densities ($n_0 < 10^{17}$), while the imaginary part depends on the actual value of the magneto-static field.

Figs. 4.8(a),(b) show that both real and imaginary parts of the input impedance decrease as n_0 increases for each gas. Furthermore, for $n_0 = 10^{16}$ m^{-3} the real, and the imaginary parts of the impedance show different values for each gas. As the plasma density rises, the difference between the impedance values for each gas reduces. At $n_0 = 10^{19}$ m^{-3} the real, and imaginary parts of the impedance have the same value for each gas.

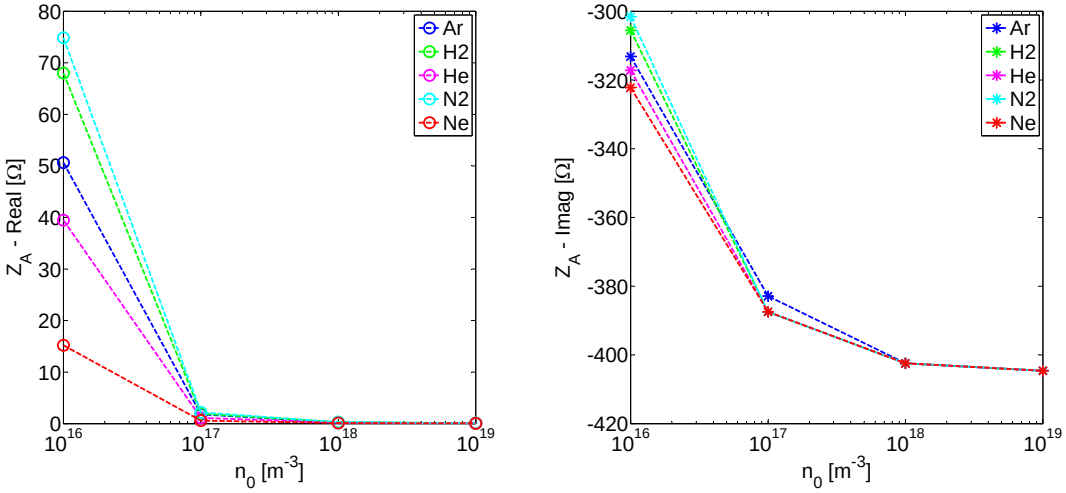

Figure 4.8: (a) Real and (b) imaginary part of the input impedance as a function of n_0 for different gas with $B_0 = 0$ mT, and $f_0 = 125$ MHz.

4.2 Plasma torus

We considered a toroidal plasma discharge placed on the yOz plane, and we computed the radiated fields due to the plasma current density contribution only. The torus has a minor radius $r = 1$ cm, and a major radius $R \approx 16$ cm. A 6 cm long metal sleeve having a 2 cm radius is placed at the bottom of the torus to drive the plasma discharge. This configuration, hereinafter referred to as *plasma torus*, is shown in Fig. 4.9.

For the numerical solution, ~ 20000 SWGs and ~ 600 RWGs were used.

We considered a non-magnetized argon plasma with an electron temperature of 3 eV, and a background neutral pressure of 15 mTorr. We assumed a uniform plasma.

In order to evaluate the performance of the plasma torus, we analyzed the radiation pattern with: (i) the plasma density n_0 in the range $10^{16} - 10^{19}$ m^{-3}, and (ii) the working frequency f_0 in the range $100 - 300$ MHz.

Figs. 4.10(a),(b) show the radiation pattern respectively on the xOz, and yOz for different values of the plasma density for a working frequency $f_0 = 300$ MHz.The plasma discharge is long approximately λ_0. Figs. 4.10(a),(b) show that the radiation pattern can be controlled in shape and intensity by adjusting the plasma density. For a density $n_0 = 10^{16}$ m^{-3} the field magnitude is lower than those for other plasma density, while for $n_0 = 10^{17}$ m^{-3} the field reaches the greatest value. Note that the radiation patterns show an asymmetry due to the presence of the excitation circuit at the bottom of the toroidal plasma discharge. At $n_0 = 10^{19}$ m^{-3} the radiation pattern resembles that of a metallic circular loop with length λ_0, except for the asymmetry already mentioned.

The radiation pattern on the $x0z$, and yOz planes of the plasma torus for different values of the working frequency is pictured in Figs. 4.11 (a),(b) for $n_0 = 10^{17}$ m^{-3}, and in

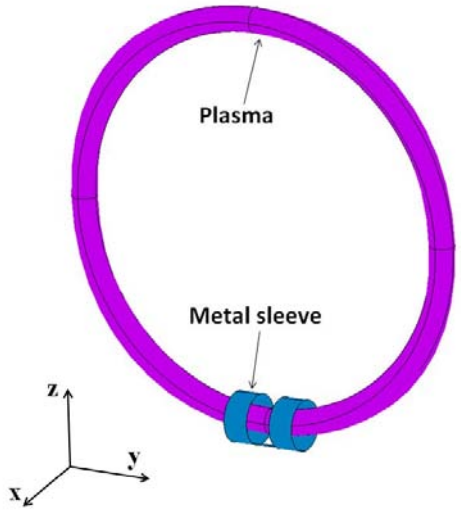

Figure 4.9: Plasma torus geometrical configuration.

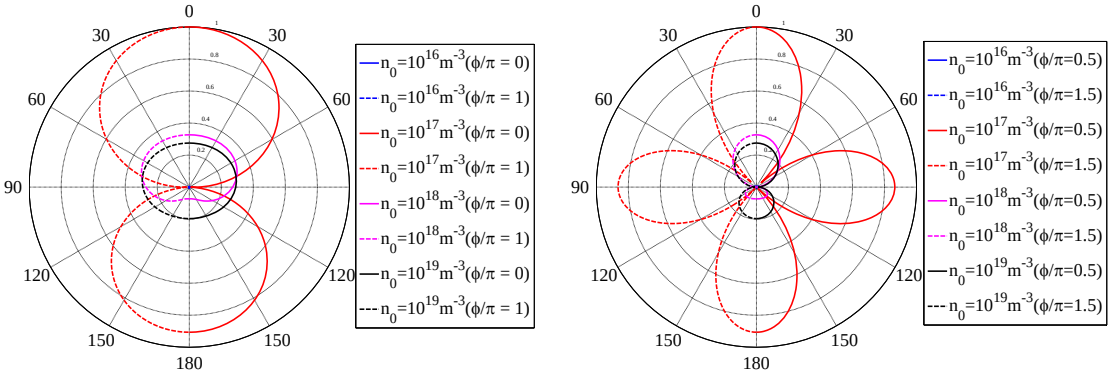

(a) (b)

Figure 4.10: Normalized radiation pattern of the plasma torus for a uniform argon plasma driven at $f_0 = 300\,\text{MHz}$ for different value of the plasma density n_0 on (a) xOz plane and (b) yOz plane.

Figs. 4.12 (a),(b) for $n_0 = 10^{19}$ m^{-3}.

Figs. 4.11(a),(b), and Figs. 4.12 (a),(b) show that the working frequency influences the radiation pattern both in magnitude and shape. The effect of the frequency variation is more evident for $n_0 = 10^{17}$ m^{-3}, at which density the intensity of the electric field with $f_0 = 100$ MHz is negligible with respect to the other frequencies.

As a circuit element, we computed the real and imaginary parts of the input impedance

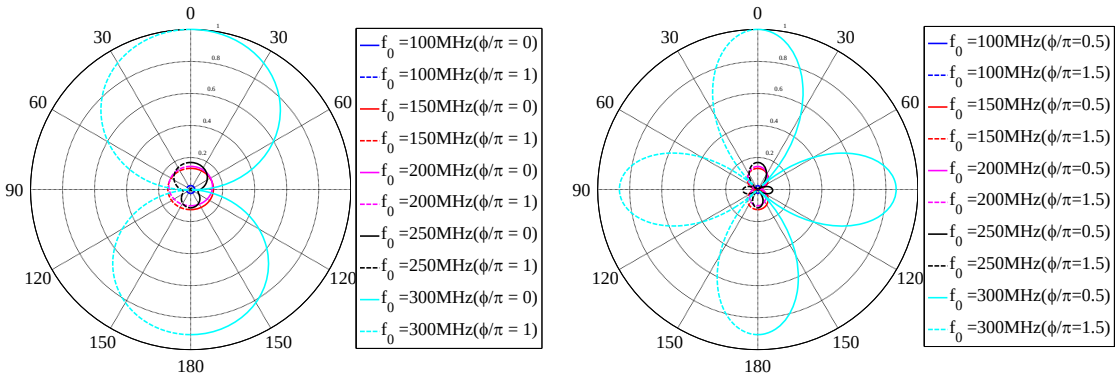

(a) (b)

Figure 4.11: Normalized radiation pattern of the plasma torus for a uniform argon plasma driven at different frequency for $n_0 = 10^{17}$ on (a) xOz plane and (b) yOz plane.

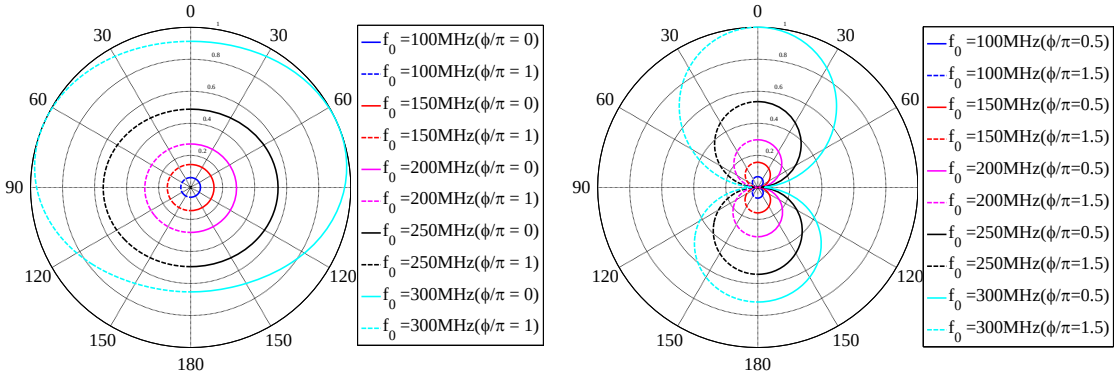

(a) (b)

Figure 4.12: Normalized radiation pattern of the plasma torus for a uniform argon plasma driven at different frequency for $n_0 = 10^{19}$ on (a) xOz plane and (b) yOz plane.

for each case considered. The results of this analysis are plotted respectively in Figs. 4.13 (a),(b).

Fig. 4.13(a) shows that the real part of the impedance has a maximum value for $n_0 = 10^{16}$ m^{-3}, and it considerably reduces for higher densities for all the frequencies considered. The imaginary part exhibits different trends for $n_0 < 10^{16}$ m^{-3}, but at higher densities assumes a constant values for each case tested, even if different in magnitude.

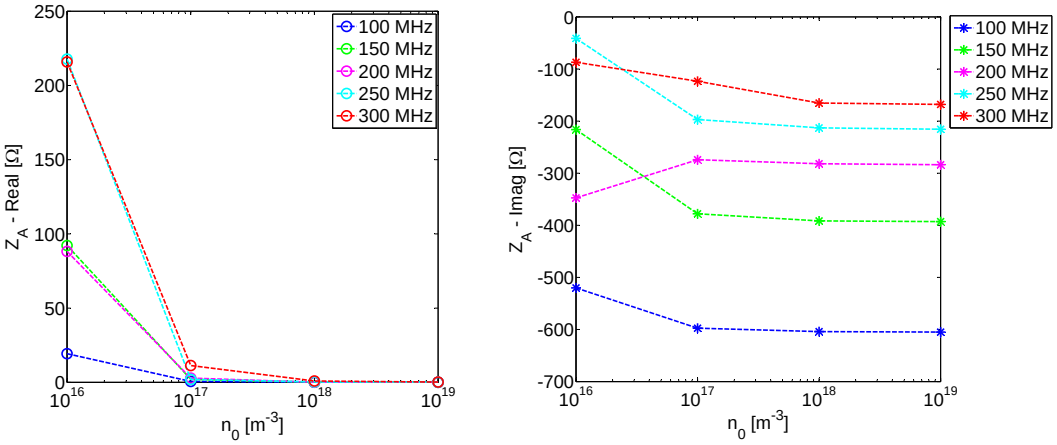

(a) (b)

Figure 4.13: (a) Real and (b) imaginary part of the input impedance as a function of n_0 for different values of f_0.

4.3 Conclusions

We considered two different configurations for GPA, and we analyzed the influence of plasma discharge parameters on the radiated field in the far field region. We simulated a plasma dipole, and a plasma torus, for radiation pattern, and input impedance taking into account the current distribution in the plasma volume only, and for different values of plasma density, working frequency, and magneto-static field. In the plasma torus configuration, no magnetic field was considered since can be hard to realize from a technological point of view.

The results obtained show that GPA can be reconfigured adjusting the plasma discharge parameters. We found out that the plasma density, and the working frequency influence the radiation pattern in shape and intensity for both configurations. The plasma dipole performance analysis on varying the operating frequency shows that the radiation pattern shape exhibit no significant variations for plasma density $n_0 \geq 10^{18}$ m^{-3}. For density lower that $< 10^{18}$ m^{-3} the radiation pattern shows sidelobes with intensity higher as the frequency increases. The field intensity has a maximum value for the highest frequency simulated (i.e. $f_0 = 200$ MHz). The same analysis on the plasma torus was performed, and it resulted that the operating frequency influences the radiation pattern both in magnitude and shape. For this configuration, the effect of the frequency variation is more evident for $n_0 = 10^{17}$ m^{-3}, at which density the intensity of the electric field with $f_0 = 100$ MHz is negligible with respect to the other frequencies. The performance analysis of the plasma dipole for different values of magneto-static field magnitude shows that the field intensity decreases as B_0 increases for $n_0 \leq 10^{17}$ m^{-3}, while the radiation pattern shape is not influenced. For higher densities, no changes were observed in both shape and field magnitude. We evaluated the plasma dipole performance when different gases are used. We considered a (i) neon, (ii) hydrogen, (iii) nitrogen, and (iv) helium

plasma. The results obtained show that the radiation pattern do not depend in shape on the gas used for the plasma column. For $n_0 \leq 10^{17}$ m^{-3}, the field intensity exhibits a gas-dependent behavior. Increasing the density, the gap between the solutions gradually reduces. For a density $n_0 = 10^{19}$ m^{-3} the field intensity is insensitive to the gas used. We evaluated the fields radiated by a uniform nitrogen plasma dipole at different values of the magneto-static field. The field intensity decreases as B_0 increases for $n_0 \leq 10^{17}$ m^{-3}, while the radiation pattern shape is not influenced. For higher densities, no changes were observed in both shape and field magnitude. At a plasma density $n_0 = 10^{19}$ the radiation patterns of both geometrical configurations in all the simulated working conditions resemble that of a geometrically corresponding metal antenna in the same working conditions. As regards the GPA as circuit elements, we computed the real and imaginary parts of the input impedance, finding out that the real part of the impedance decreases as the plasma density rises for both geometrical configurations, and for all the working conditions considered.

Chapter 5

Plasma antennas

In the previous chapter, we evaluated the scattered electric field neglecting the current distribution on the metal surface, as we were interested in the plasma response only. In this chapter we computed the radiation pattern considering the contribution of the current density in the plasma volume and on the metal surface, in order to investigate the performance of the plasma device as an antenna. To this purpose we simulated a plasma dipole, and we analyzed the influence of the driving circuit geometry, and of the working frequency on its performance. Subsequently, we studied the GPA behavior when stacked into array simulating a GPA array, and we analyzed its performance in terms of gain and directivity at different working frequencies, taking into account the current distributions in the plasma volumes and on the metal surfaces.

5.1 Driving circuit

We considered a plasma dipole with the axis aligned along the $\hat{\boldsymbol{z}}$ direction. The dipole is 7.5 cm long, and its radius is 1.25 mm. We considered a uniform argon plasma, with $n_0 = 10^{19}$ m^{-3}, a background neutral pressure of 15 mTorr, and a working frequency $f_0 = 2$ GHz, so the dipole is $\lambda_0/2$ electrically long. No magnetic field was considered. We analyze the dipole performance when geometrically different driving circuits are considered. We simulated:

1. a 3.7 mm long metallic sleeve with a 1.75 mm radius ($\sim$ 1000 RWGs), shown in Fig. 2.2, and referred to as *half-nagoya*;

2. a 0.5 mm long metallic loop ($\sim$ 80 RWGs) shown in Fig. 5.1(a), having a 1.75 mm radius, and refered to as *single-loop*;

3. two identical 0.5 mm long loops ($\sim$ 80 RWGs each), placed at a distance equal to their radius, that is 1.75 mm long. This configuration will be referred to as *double-loop*, and it is pictured in Fig. 5.1(b).

The gain, and directivity resulting from the analysis with different driving circuit geometries are respectively shown in Figs. 5.2(a),(b),(c), and in Figs. 5.3(a),(b),(c).

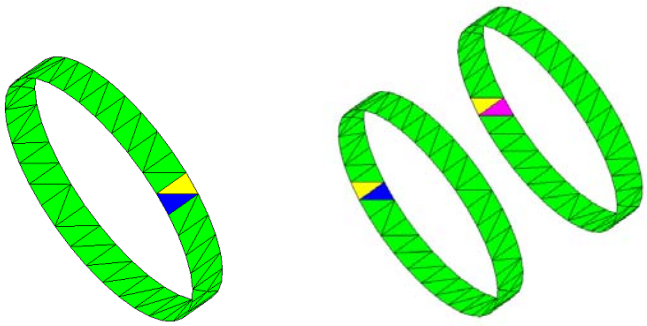

(a) (b)

Figure 5.1: Two driving circuit meshes, a (a) *single-loop*, and (b) *double-loop* with material property definitions. Note that the *double-loop* has two ports (in blue, and purple).

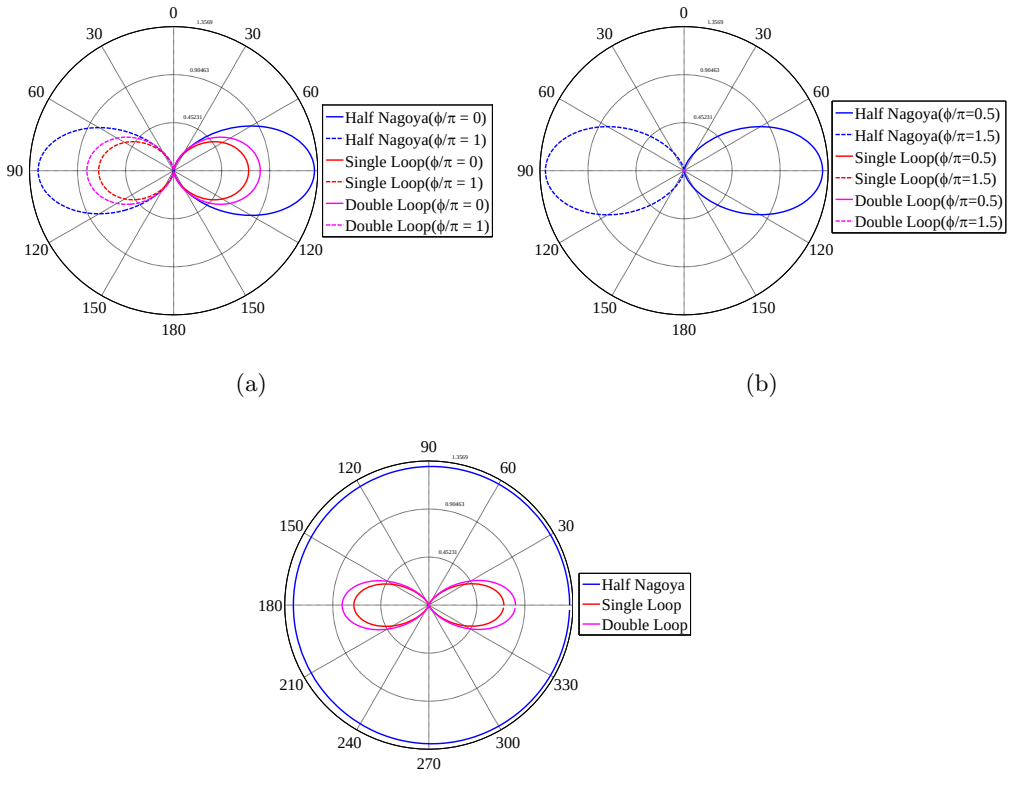

(a) (b)

(c)

Figure 5.2: Gain of a plasma dipole with $n_0 = 10^{19}$ m^{-3}, driven at $f_0 = 2$ GHz by different driving circuit geometries on (a) xOz, (b) yOz, and (c) xOy planes ($G_{max} = 1.3560$).

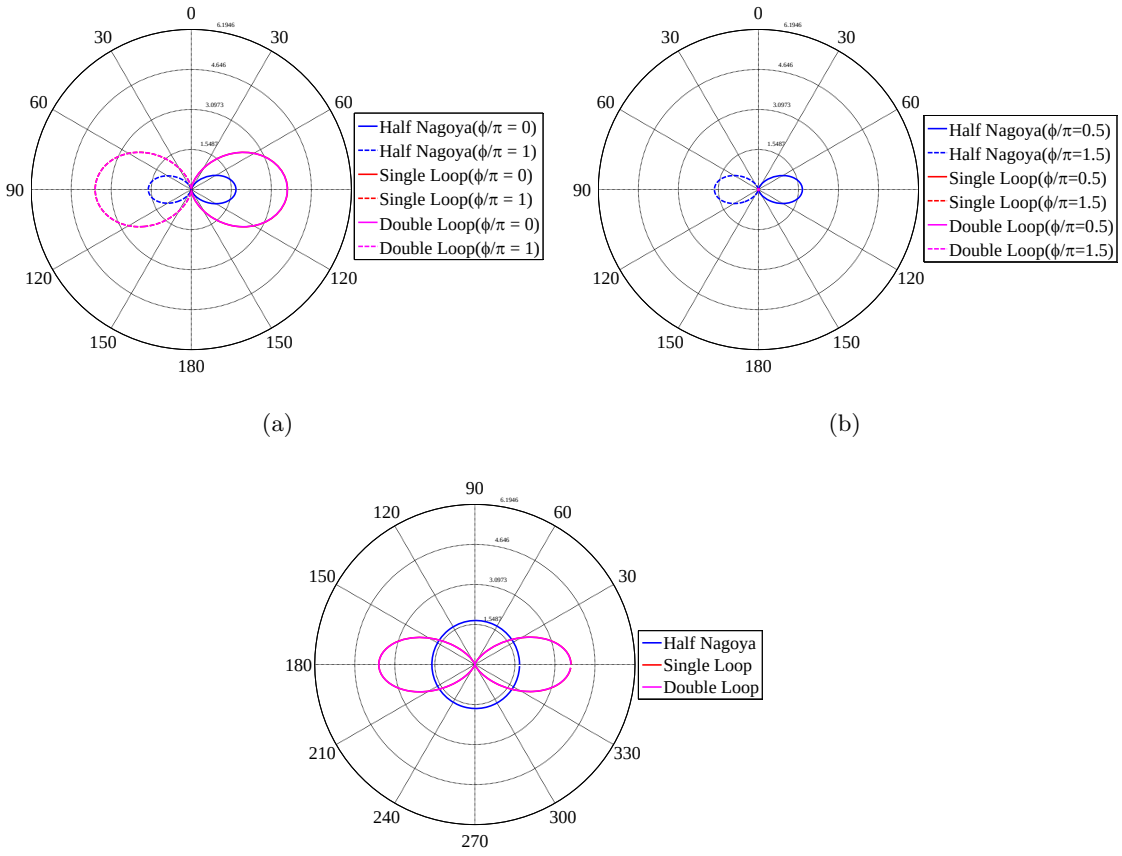

Figure 5.3: Directivity of a plasma dipole with $n_0 = 10^{19}$ m^{-3}, driven at $f_0 = 2$ GHz by different driving circuit geometries on (a) xOz, (b) yOz, and (c) xOy planes ($D_{max} = 6.1946$).

Figs. 5.2(a),(b),(c), and Figs. 5.3(a),(b),(c) show that the gain and directivity patterns vary both in shape, and magnitude as the geometry of the driving circuit does so. The gain reaches its maximum value for the *half-nagoya* circuit. The gain patterns of the *single-loop*, and of the *double-loop* are similar in both shape and magnitude, and on the yOz plane the gain of these configurations are negligible with respect to the *half-nagoya*. The directivity has a maxumim for the *double-loop* driving circuit on the xOz, and on the xOy planes, while on the plane yOz it is negligible with respect to the *half-nagoya* case. The directivity of the dipole driven by the *single-loop* is negligible with respect the other cases. It is worth to be noted that the patterns for plasma dipole driven by the *single-loop*, and by the *double-loop* are different from the patterns of a metal $\lambda_0/2$ dipole.

We evaluated the radiated fields of the plasma dipole driven by three *half-nagoya* with different lengths, respectively 3.7, 7.4, and 11.1 mm. The nagoya have the same 1.75 mm

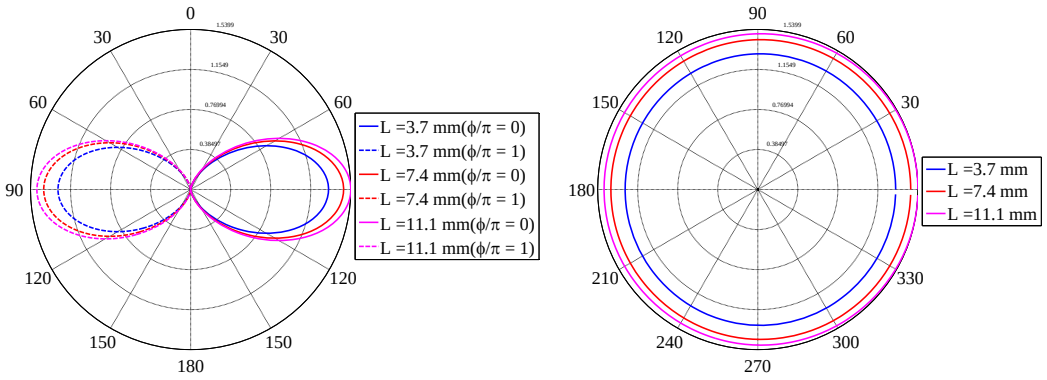

(a) (b)

Figure 5.4: Gain of a plasma dipole with $n_0 = 10^{19}$ m^{-3}, driven at $f_0 = 2$ GHz by three *half-nagoya* different in length on (a) xOz, (b) xOy planes ($G_{max} = 1.5399$).

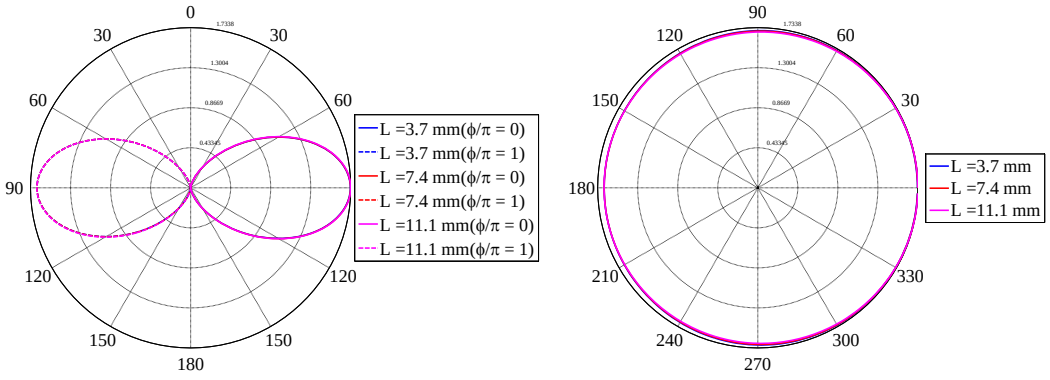

(a) (b)

Figure 5.5: Directivity of a plasma dipole with $n_0 = 10^{19}$ m^{-3}, driven at $f_0 = 2$ GHz by *half-nagoya* different in length on (a) xOz, (b) xOy planes ($D_{max} = 1.7338$).

radius, and they are simulated using ~ 1000 RWGs for the first two, and ~ 1500 RWGs for the latter. The gain, and the directivity obtained on the xOz, and xOy planes are plotted in Figs. 5.4(a),(b), and Figs. 5.5(a),(b). Figs. 5.4(a),(b), and Figs. 5.5(a),(b) show that the gain patterns are similar in shape but different in magnitude, while the directivity patters are the same. The gain has its maximum value when the dipole is driven by the 11.1 mm long *half-nagoya*, and decrease as the length of the driving circuit does so. Note that the patters resemble that of a metal $\lambda_0/2$ dipole.

5.2 Plasma dipole antenna

We analyzed the performance in terms of gain and directivity of the plasma dipole driven at $f_0 = 2$ GHz by the *half-nagoya* circuit. The results obtained were compared with that obtained for the corresponding ideal PEC $\lambda_0/2$ dipole. The latter was simulated by means of ADAMANT as a cylindrical PEC surface excited in its middle circumference as shown in Figs. 5.6(a),(b).

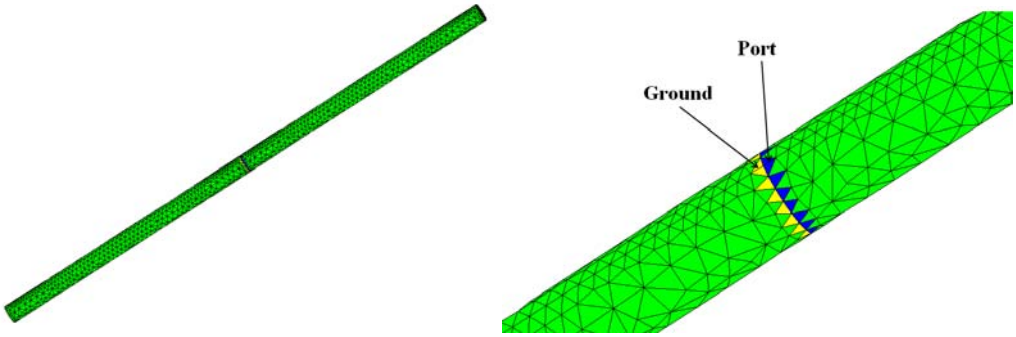

(a) (b)

Figure 5.6: (a) The ideal PEC dipole mesh, and (b) enlarged view of the feeding region.

The resulting gain on xOz, xOy planes are shown in Figs. 5.7(a),(b) respectively, while the directivity on the same planes is plotted in Figs. 5.8(a),(b), as both gain and directivity patterns on xOz and on yOz are the same.

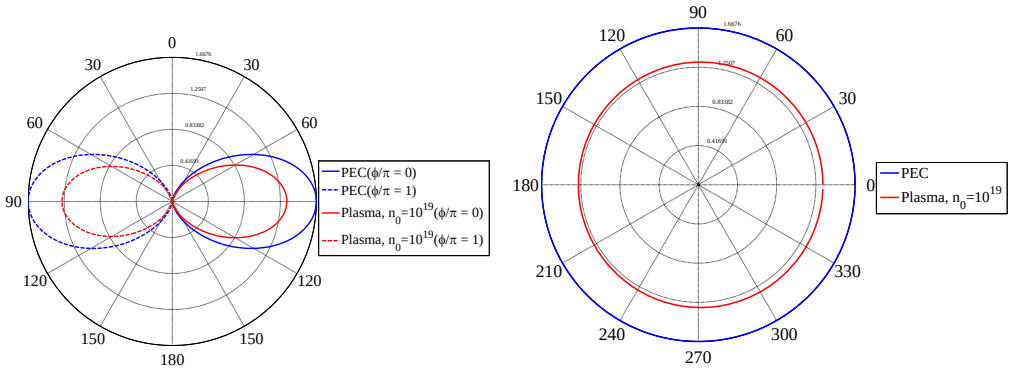

(a) (b)

Figure 5.7: Gain of a plasma dipole driven at $f_0 = 2$ GHz, with $n_0 = 10^{19}$ m^{-3} with respect to the corresponding PEC dipole on (a) xOz, and (b) xOy planes ($G_{max} = 1.6676$).

As can be seen from Figs. 5.7(a),(b), and Figs. 5.8(a),(b), the gain and directivity patterns of the plasma dipole, and of the PEC dipole are equal in shape, except for an

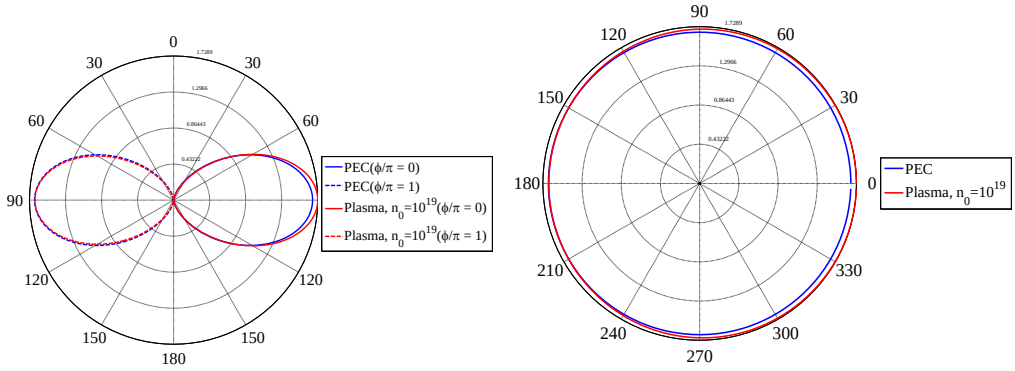

(a) (b)

Figure 5.8: Directivity of a plasma dipole driven at $f_0 = 2$ GHz, with $n_0 = 10^{19}$ m^{-3} with respect to the corresponding PEC dipole on (a) xOz, and (b) xOy planes ($D_{max} = 1.7289$).

asymmetry in the plasma dipole patterns due to the presence of the driving circuit. It is worth to be noted that the PEC dipole gain is higher than the plasma dipole gain, while the directivity has higher value for the plasma dipole than for the PEC dipole, as shown in Figs. 5.8(a),(b). This is due to power loss related to the power absorbed by the plasma.

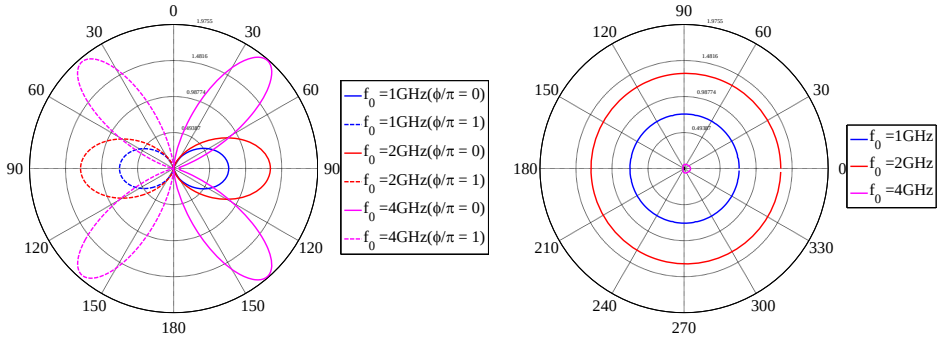

(a) (b)

Figure 5.9: Gain of a plasma dipole with $n_0 = 10^{19}$ m^{-3} driven at different frequencies on (a) xOz, and (b) xOy planes ($G_{max} = 1.9755$).

We analyzed the performance of the plasma dipole with $n_0 = 10^{19}$ m^{-3} when different working frequency are considered. The gain for $f_0 = 1$, 2, and 4 GHz are shown in Figs. 5.9(a),(b), and the directivity in Figs. 5.10(a),(b), respectively on the xOz, xOz planes. As can be seen from Figs. 5.9(a),(b), and from Figs. 5.10(a),(b), the plasma dipole gain and directivity on the xOz (and yOz) plane rises as the working frequency increases, reaching their maximum values for $f_0 = 4$ GHz. The gain has its maximum on the xOz

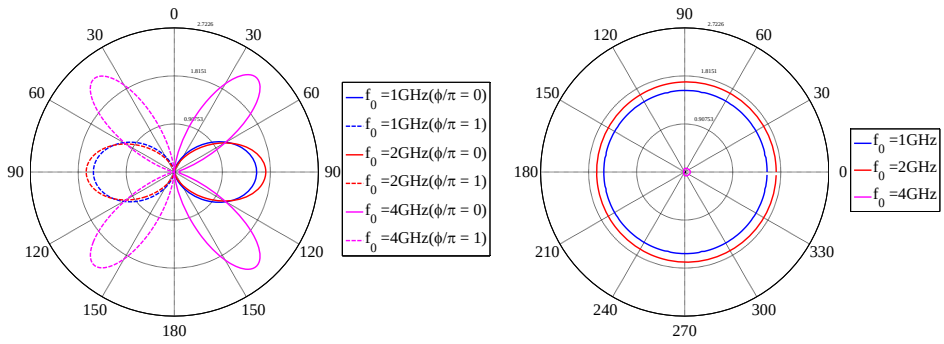

(a) (b)

Figure 5.10: Directivity of a plasma dipole with $n_0 = 10^{19}$ m^{-3} driven at different frequencies on (a) xOz, and (b) xOy planes ($D_{max} = 2.7226$).

(yOz) plane, while the directivity do not has its maximum on one of the principal planes. Note that the change of gain and directivity with the frequency resembles that of a PEC dipole.

5.3 Plasma array antenna

We considered two plasma dipoles, placed on the xOz plane with their axis aligned in the $\hat{\boldsymbol{z}}$ direction, and both 7.5 cm long. They are placed at $x = -3.75$ cm and $x = +3.75$ cm respectively, so that the distance between them is equal to 7.5 cm along the $\hat{\boldsymbol{x}}$ direction, as shown in Fig. 5.11. Hereinafter this configuration will be referred to as *plasma array*. We considered a uniform argon plasma, with $n_0 = 10^{19}$ m^{-3}, and a background neutral pressure of 15 mTorr.

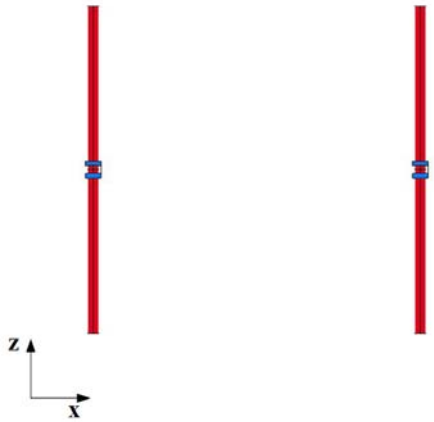

Figure 5.11: Plasma array geometrical configuration.

We analyzed the plasma array antenna performance in terms of gain and directivity at different working frequencies, taking into account the current distributions in the plasma volumes and on the metal surfaces, and when the dipoles are excited in phase, and in phase opposition. The results on principal planes xOz, yOz, and xOy for the gain, and the directivity are shown in Figs. 5.12(a),(b),(c), and in Figs. 5.13(a),(b),(c), respectively. Both gain and directivity reach their maximum values on the yOz plane, but the first for a driven frequency $f_0 = 4$ GHz, while the latter for $f_0 = 10$ GHz. On the xOy plane, gain and directivity are negligible for $f_0 > 2$ GHz. The pattern changes in shape and intensity with the frequency, just like a metallic array does.

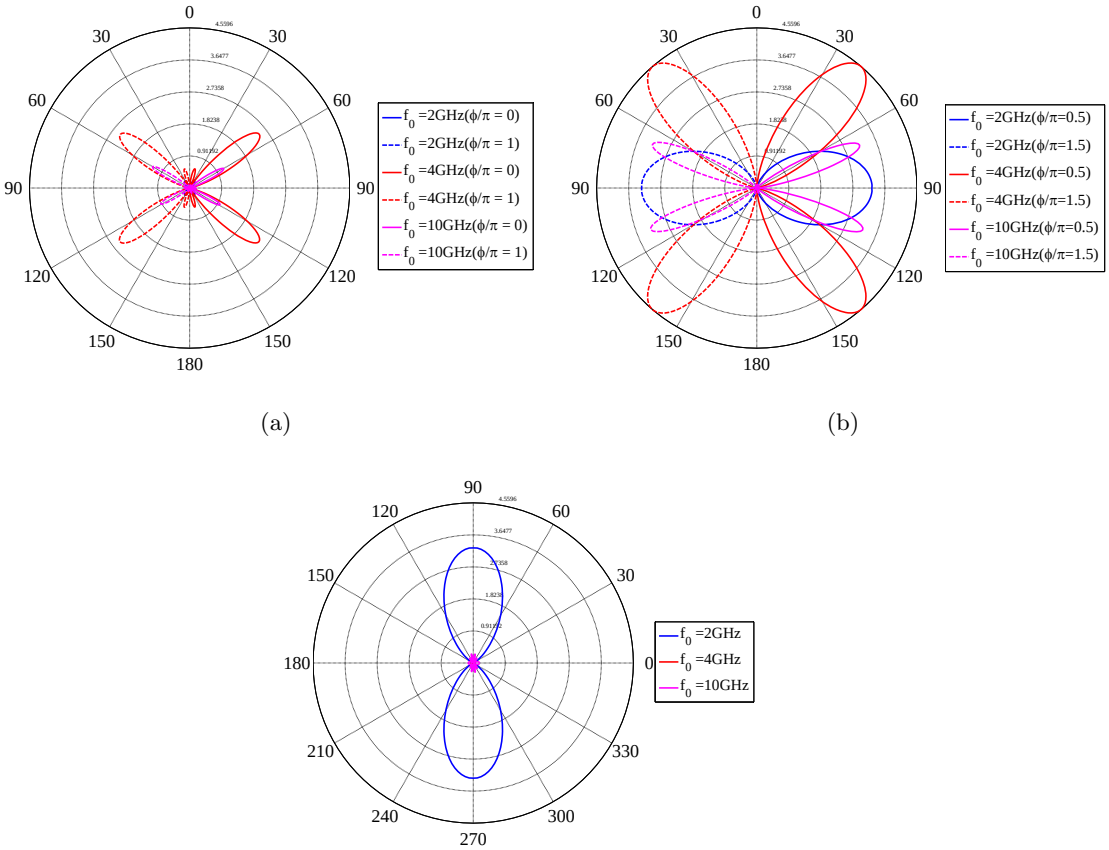

(a) (b)

(c)

Figure 5.12: Gain of a parallel plasma array with $n_0 = 10^{19}$ m^{-3}, and the dipoles fed in phase, driven at different frequencies on (a) xOz, (b) yOz, and (c) xOy planes ($G_{max} = 4.5596$).

The results on the main planes for the gain, and the directivity at different working frequencies when the dipoles are excited in phase opposition are shown in Figs. 5.14(a),(b),(c), and in Figs. 5.15(a),(b),(c), respectively.

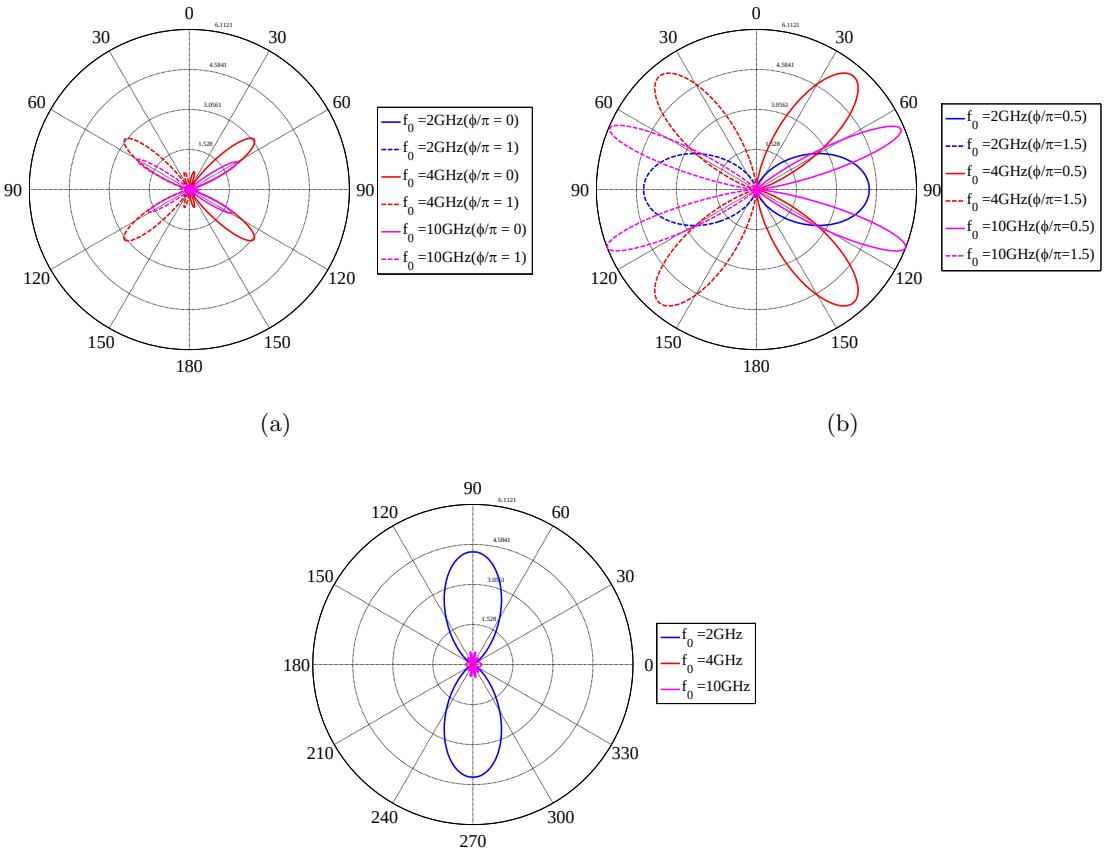

Figure 5.13: Directivity of a parallel plasma array with $n_0 = 10^{19}$ m^{-3}, and dipoles fed in phase, driven at different frequencies on (a) xOz, (b) yOz, and (c) xOy planes ($D_{max} = 6.1121$).

From Figs. 5.14(a),(b),(c), and Figs. 5.15(a),(b),(c) can be seen that the gain and the directivity on yOz plane are negligible with respect to the other planes, while for frequencies higher than > 2 GHz they are negligible on all the planes but on the xOz plane. The gain is higher for $f_0 = 4$ GHz than for other frequencies, whereas the directivity has its maximum value for $f_0 = 10$ GHz. Note that the gain and the directivity do not have their maximum values on the principal planes.

It is worth to be noted how the maximum value for both gain and directivity moves with the phase shift between the dipole feedings. Moreover, the gain and directivity maximums are in the yOz plane when the dipoles are fed in phase, while gain and directivity become negligible on the same plane when the dipole are excited in phase opposition.

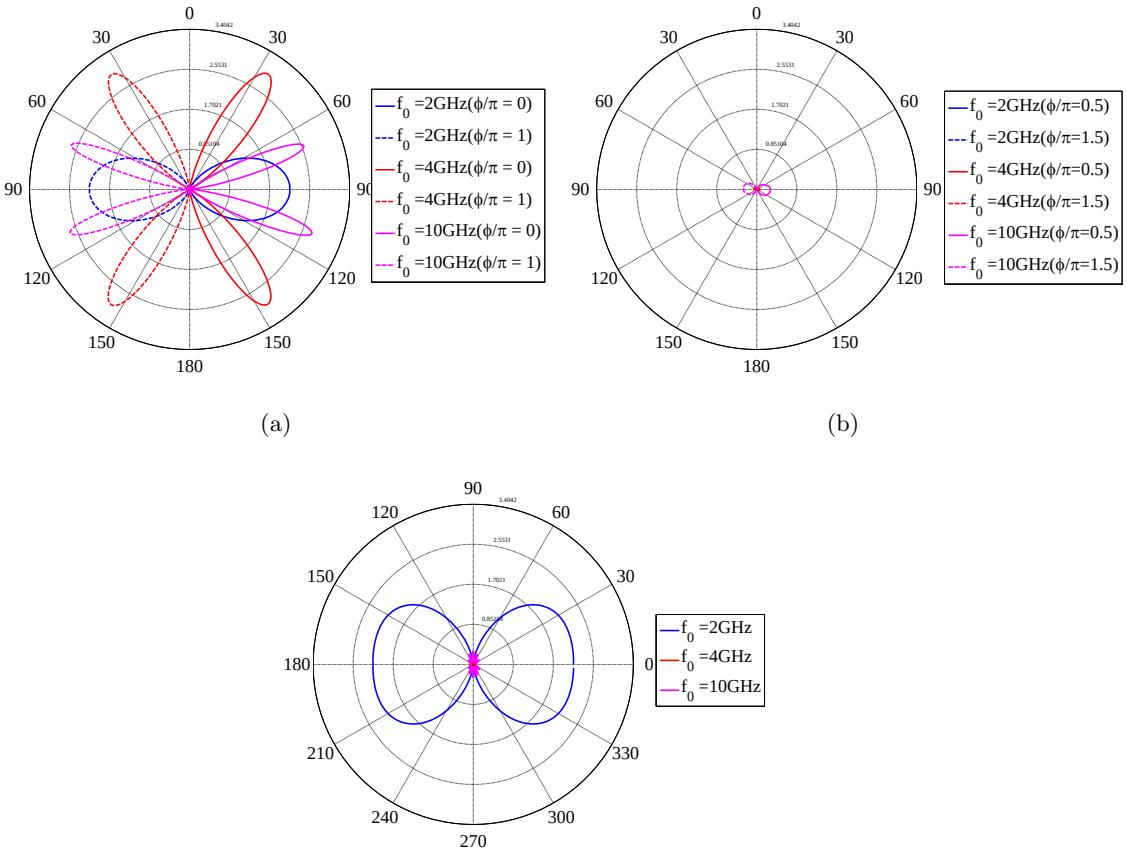

Figure 5.14: Gain of a parallel plasma array with $n_0 = 10^{19}$ m^{-3}, and dipoles fed in antiphase, driven at different frequencies on (a) xOz, (b) yOz, and (c) xOy planes ($G_{max} = 3.4042$).

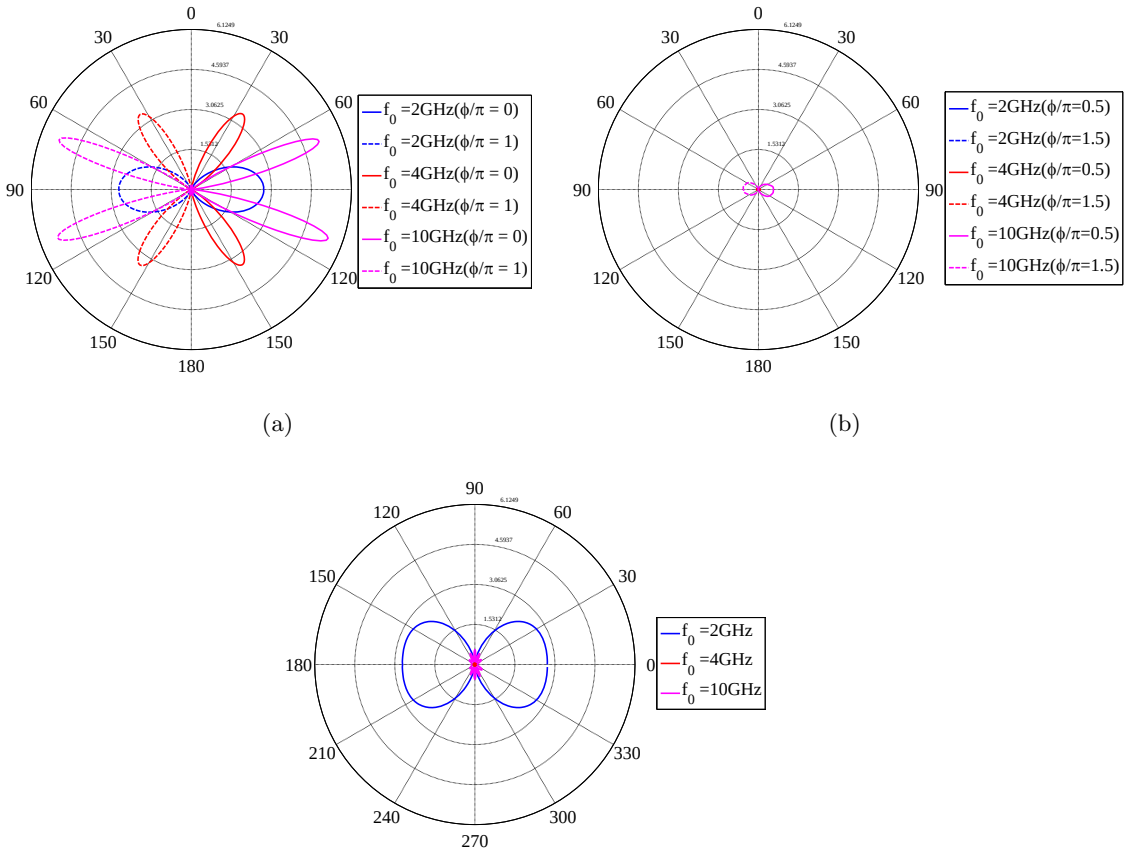

Figure 5.15: Directivity of a parallel plasma array with $n_0 = 10^{19}$ m^{-3}, and dipoles fed in antiphase, driven at different frequencies on (a) xOz, (b) yOz, and (c) xOy planes ($D_{max} = 6.1249$).

5.4 Conclusions

In order to investigate the performance of the plasma device as an antenna, we simulated a plasma dipole, and we computed the radiated field due to the current distributions in the plasma volume and on the metal surface. In this analysis we considered a uniform argon plasma with $n_0 = 10^{19}$ m^{-3}, and a neutral pressure of 15 mTorr.

We wanted firstly to analyzed how the driving circuit affect the GPA performance. To this purpose, we simulated a plasma dipole driven by: (i) three *half-nagoya* of different length, a (ii) *single-loop*, and a (iii) *double-loop* excited in phase. We computed gain and directivity for each configuration. We found out that the gain, and directivity patterns are subjected to variation in both shape, and intensity as the driving circuit geometry changes. The gain patterns of a plasma dipole driven by the *single-loop*, and *double-loop* are similar in shape, and they have intensity negligible on yOz plane with respect to

the *half-nagoya* case. The gain increases as the *half-nagoya* length does so, reaching its maximum for the longest *half-nagoya* simulated (i.e. 11.1 mm long), while the directivity pattern in insensitive to *half-nagoya* length variations.

We then simulated a plasma dipole driven at different frequencies by a *half-nagoya* circuit, and we computed gain and directivity. The results were compared with that obtained by simulating a PEC dipole in the same working conditions. We assessed that the plasma dipole has directivity higher than the directivity of the PEC dipole, but a lower gain. This is due to power loss related to the power absorbed by the plasma. It was shown that the plasma dipole has maximum values for gain and directivity for the higher frequency simulated (i.e. $f_0 = 4$ GHz). Varying the working frequency it is possible to adjust gain and directivity patterns in both shape and magnitude.

In order to evaluate the GPA behavior when stacked into arrays, we simulated a plasma array composed by two identical plasma dipole parallely placed. The dipoles are fed in phase, and phase opposition. The results obtained for the plasma array show that it is possible to adjust gain and directivity patterns in both shape and magnitude varying the working frequency, just like a metallic array. The plasma array has higher values of gain when the dipoles are excited in phase than in phase opposition. When the dipoles are excited in phase, both gain and directivity have maximum on the yOz plane, but the former for $f_0 = 4$ GHz, and the latter for $f_0 = 10$ GHz. varying the phase shift between the excitation, the maximum value for both gain and directivity moves from the yOz plane toward the xOz plane. When the dipoles are fed in phase opposition, both gain and directivity are negligible on the yOz, and xOy planes with respect to the results on the xOz plane for frequencies higher than > 2 GHz. This behavior resembles that of a corresponding metal array.

Chapter 6

Conclusions

In this work we considered GPAs, devices that rely on a partially or fully ionized gas to radiated EM, rather than metallic part as traditional antennas. Potentially, plasma antennas have the following advantages on metallic antennas: (i) GPAs are reconfigurable with respect to their impedance, radiation pattern, working frequency, and bandwidth; (ii) they can be reconfigured electrically on time scales the order of microseconds to milliseconds; (iii) they are energized only while the communication takes place, so they have lower thermal noise and minimize signal degradation; (iv) they are virtually *transparent* above the plasma frequency and become *invisible* once turned off.

Up to now several analytical and numerical models have been developed to study plasma antennas, and FDTD method has been more recently used to compute plasma antenna parameters [25], [26], and its radiation characteristics taking into account plasma density profiles, and an external magneto-static field. However, this numerical methods rely on simplified plasma models allowing for simplified antenna analysis.

ADAMANT, a full-wave numerical tool based on a set of coupled surface and volume integral equations for the driving circuit, and the plasma discharge, respectively, was used to investigate the influence of plasma parameters in the performance of GPA. This approach allows the accurate computation of the current distribution on the driving circuit and in the plasma, thus enabling the evaluation of input impedance, radiation pattern, gain, and directivity.

We analyzed two different GPA configuration: a plasma dipole, and a plasma torus. Since the numerical result accuracy depends upon the number of RWGs, and SWGs used to simulate the driving circuit, and the plasma volume respectively, we performed a convergence analysis on each configuration. To this purpose, we simulated several meshes of the metal surface, and of the plasma volume for the radiation patters, and input impedance, and we compared the results obtained expecting to find an asymptotic behavior. We found out the the driving parameters in assessing the number of RWGs and SWGs are: (i) the working frequency, (ii) the geometry, and (iii) the plasma discharge parameters. As RWGs and SWGs are defined on triangular and tetrahedral elements, the requirements on the number of RWGs and SWGs can be translated into requirements on the mesh patches: (i) at least 10 triangular (tetrahedral) mesh element for each λ_0, (ii) the areas of the metal surface mesh triangles, and that of the tetrahedron facets in the plasma volume should be as similar as possible. For both configurations, we simulated three plasma volume meshes

with different numbers of SWGs for a given number of RWGs, obtaining the radiation pattern and input impedance due to the plasma current distribution. Then we simulated three meshes of the driving circuit with different RWG numbers for a given volume mesh, and we evaluate the scattered fields due to the current distribution in the plasma volume, and on the metal surface. The results obtained show that the solution has an asymptotic behavior with respect to the SWG, and RWG numbers. Moreover, increasing the RWG number can lead to numerical instabilities, which destroy the accuracy of the current distribution over the metal surface.

We first wanted to assess the influence of the plasma discharge parameters on the performance of GPAs. To this purpose we considered a plasma dipole, and a plasma torus, both filled with a uniform argon plasma having an electron temperature of 3 eV, and a background neutral pressure of 15 mTorr, and we computed the radiated field due to the plasma current distribution only for different working conditions.

For the plasma dipole, we evaluated the radiated fields in term of shape and field intensity on varying: (i) the plasma density, (ii) the working frequency f_0, and (iii) the external magneto-static field B_0. We assessed that the radiation pattern can be controlled both in shape and magnitude by adjusting the plasma density. For high plasma densities (i.e. $n_0 \geq 10^{19}$ m^{-3}) the plasma dipole radiation pattern resemble that of a corresponding $\lambda_0/2$ metal dipole. The plasma dipole performance analysis on varying the operating frequency shows that the radiation pattern shape exhibit no significant variations for plasma density $n_0 \geq 10^{18}$ m^{-3}. However, for densities lower than $< 10^{18}$ m^{-3} the radiation pattern shows sidelobes with intensity higher as the frequency increases. The field intensity can be changed adjusting the frequency, and it has a maximum value for the highest frequency simulated (i.e. $f_0 = 200$ MHz). We also assessed the influence of the gas chosen on the performance of the plasma dipole, computing the radiation pattern for a (i) neon, (ii) hydrogen, (iii) nitrogen, and (iv) helium plasma with an electron temperature of 3 eV, and a background neutral pressure of 15 mTorr. This analysis shows that the radiation pattern shape is insensitive to the gas used for the plasma column. For $n_0 \leq 10^{17}$ m^{-3}, the field intensity exhibits a gas-dependent and a density-dependent behavior. Increasing the density, the gap between the solutions gradually reduces. For a density $n_0 = 10^{19}$ m^{-3} the field intensity does not depend on the gas chosen.

We computed the field radiated by the plasma torus on varying: (i) the plasma density, (ii) the working frequency f_0. For this geometrical configuration, no magneto-static field was considered since difficult to obtain from a technological point of view. The analysis results show that it is possible to reconfigure the radiation pattern in both shape and intensity by changing the plasma density. The field intensity has its maximum for $n_0 = 10^{17}$ m^{-3}, while for $n_0 = 10^{16}$ m^{-3} it is negligible with respect to other densities. For plasma densities $n_0 \geq 10^{19}$ m^{-3} the plasma torus radiation pattern resemble that of a corresponding metal loop except for an asymmetry due to presence of the driving circuit at the bottom of the plasma discharge. The analysis on the plasma torus performance when driven at different frequencies resulted that the operating frequency influences the radiation pattern both in magnitude and shape. The effect of the frequency variation is more evident for $n_0 = 10^{17}$ m^{-3}, at which density the field intensity when the plasma is driven at $f_0 = 100$ MHz is negligible with respect to the other cases.

As regards GPAs as circuit elements, we computed the real and imaginary parts of

the input impedance, showing that the real part decreases as the plasma density rises for both geometrical configurations, and for all the working conditions considered.

We analyzed how the driving circuit geometry affects the GPA performances. We considered a plasma dipole driven by: (i) three *half-nagoya* of different length, a (ii) *single-loop*, and a (iii) *double-loop* excited in phase. We computed gain and directivity for each configuration taking into account the current distributions in the plasma volume and on the metal surface. In this analysis we assumed a uniform argon plasma with $n_0 = 10^{19}$ m^{-3}, and a neutral pressure of 15 mTorr. The results obtained show that:

- the gain, and directivity patterns are subjected to variation in both shape, and intensity as the driving circuit geometry changes;
- the gain patterns of a plasma dipole driven by the *single-loop*, and *double-loop* are similar in shape, and on yOz plane they have intensity negligible with respect to the *half-nagoya* case;
- the directivity pattern in the *single-loop* case have intensity negligible with respect to the other driving circuits;
- the gain increases as the *half-nagoya* length does so, reaching its maximum for the longest *half-nagoya* simulated (i.e. 11.1 mm long);
- the directivity pattern is insensitive to the length of the *half-nagoya*.

Subsequently, we evaluated the performance of the plasma device as an actual antenna. To this purpose we simulated a plasma dipole driven at different frequencies by a *half-nagoya* circuit, and we computed gain and directivity considering the current distributions on the metal surface and in the plasma volume. We considered a uniform argon plasma with $n_0 = 10^{19}$ m^{-3}, and a neutral pressure of 15 mTorr. The results were compared with that obtained by simulating a PEC dipole in the same working conditions. We assessed that the plasma dipole has directivity higher than the directivity of the PEC dipole, but a lower gain. This is due to power loss related to the power absorbed by the plasma. It was shown that the plasma dipole has maximum values for gain and directivity for the higher frequency simulated (i.e. $f_0 = 4$ GHz). Varying the working frequency it is possible to adjust gain and directivity patterns in both shape and magnitude.

Finally, we analyzed the GPA behavior when stacked into arrays. We simulated a plasma array composed by two identical plasma dipole parallely placed. The dipoles are excited in phase, and in phase opposition. The results obtained for the plasma array show that it is possible to adjust gain and directivity patterns in both shape and magnitude varying the working frequency, just like a metallic array. The plasma array has higher values of gain, and directivity on the xOz plane when the dipoles are fed in phase than in phase opposition. When the dipoles are excited in phase, both gain and directivity have maximum on the yOz plane, but the former for $f_0 = 4$ GHz, and the latter for $f_0 = 10$ GHz. Varying the phase shift between the excitation, the maximum value for both gain and directivity moves from the yOz plane toward the xOz plane. When the dipoles are fed in phase opposition, both gain and directivity are negligible on the yOz, and xOy planes with respect to the results on the xOz plane for frequencies higher than > 2 GHz. This behavior resembles that of a corresponding metallic array.

Through these investigations, we assessed that GPAs are similar to metal antennas when the plasma density is high enough (i.e. $n_0 \geq 10^{19}$ m^{-3}). However, it is possible to reconfigure the radiation pattern in both shape and intensity by varying (i) the plasma density, (ii) the working frequency, and (iii) the magneto-static field (if present). These reconfiguration capabilities give to plasma antenna some advantages over metal antennas, and make GPAs being a promising alternative in many applications (i.e. multiband antennas, phased array, beam-forming antennas, reflectors).

Appendix A

The Rao-Wilton-Glisson basis function

The expression of nth RWG basis function defined on two adjoining triangles T_n^+ and T_n^- connected through the nth common edge is [37]

$$\boldsymbol{f}_n(\boldsymbol{r}) = \begin{cases} \frac{l_n}{2A_n^+}\boldsymbol{\rho}_n^+ & , \boldsymbol{r} \in T_n^+ \\ \\ \frac{l_n}{2A_n^-}\boldsymbol{\rho}_n^- & , \boldsymbol{r} \in T_n^- \end{cases} \tag{A.1}$$

where $\boldsymbol{\rho}_n^\pm$ are the position vectors with respect to triangular vertices $O_n^\pm$, $\boldsymbol{r}$ is the position vector with respect to the global origin O, $A_n^\pm$ is the area of triangle $T_n^\pm$, and l_n is the length of the common edge, as shown in Figs. A.1(a), (b).

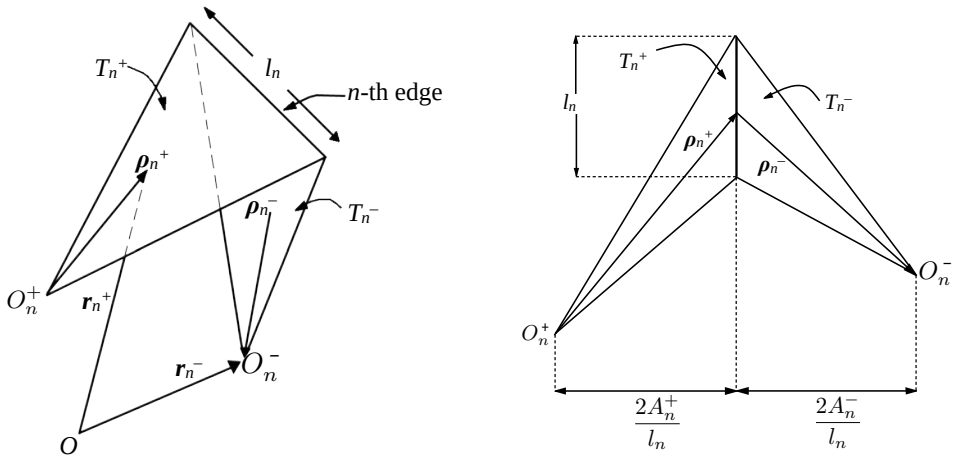

Figure A.1: Geometrical parameters associated with the nth RWG basis function, with (a) triangle pair and geometrical parameters associated with interior edge, and (b) geometry for construction of component of basis function normal to the edge.

The basis function $\boldsymbol{f}_n$ is used to approximately represent the surface current, and some of its properties are:

1. The normal component of the current is continuous across the common edge, and the current component normal to the boundary of the surface formed by $T_n^+ \cup T_n^-$ is zero. Consequently, no line charges are present along the common (interior) edge and along the outer boundary of the RWG function. Moreover the surface divergence in $T_n^\pm$ of $\boldsymbol{f}_n$ is proportional to the surface charge density associated with the triangular patch, and it is

$$\nabla_S \cdot \boldsymbol{f}_n(\boldsymbol{r}) = \begin{cases} \frac{l_n}{A_n^+} & , \boldsymbol{r} \in T_n^+ \\ -\frac{l_n}{A_n^-} & , \boldsymbol{r} \in T_n^- \\ 0 & , \text{otherwise} \end{cases} \tag{A.2}$$

   We can conclude that the surface charge density is constant within a single triangle, and the total charge associated with the triangle pair $T_n^\pm$ is zero.

2. The normal component on the boundary of $T_n^+ \cup T_n^-$ is zero.

3. The moment of $\boldsymbol{f}_n(\boldsymbol{r})$ is

$$\left(A_n^+ + A_n^+\right) \boldsymbol{f}_n^{avg}(\boldsymbol{r}) \equiv \int_{T_n^+ \cup T_n^-} \boldsymbol{f}_n(\boldsymbol{r})\, dS = \frac{l_n}{2}\left(\boldsymbol{\rho}_n^{c+} + \boldsymbol{\rho}_n^{c-}\right) = l_n\left(\boldsymbol{r}_n^{c+} + \boldsymbol{r}_n^{c-}\right) \tag{A.3}$$

   where $\boldsymbol{\rho}_n^{c\pm}$ is the vector between the free vertex and the centroid of $T_n^\pm$, with $\boldsymbol{\rho}_n^{c+}$ directed toward and $\boldsymbol{\rho}_n^{c-}$ directed away from the common edge l_n. The vector from the global origin O to the centroid of $T_n^\pm$ is represented by $\boldsymbol{r}_n^{c\pm}$.

We can approximate the current on the metal surface in terms of the $\boldsymbol{f}_n$ as

$$\boldsymbol{J_A} \cong \sum_{n=1}^{N} I_n \boldsymbol{f}_n(\boldsymbol{r}) \tag{A.4}$$

where N is the number of interior (nonboundary) edges. Each nonboundary edge of the mesh is associated with a basis function, so up to three basis functions may have nonzero walues within each triangular patch. Moreover, at a given edge only the basis function associated with that edge has a nonzero current component normal to the edge, since all other basis functions in adjacent patches are parallel to the edge.

Appendix B

The Schaubert-Wilton-Glisson basis function

The expression of pth SWG basis function defined on two adjoining tetrahedrons Ω_p^+ and Ω_p^- connected through the shared facet is [38]

$$\boldsymbol{v}_p(\boldsymbol{r}) = \begin{cases} \frac{A_{4p}}{3V_p^+}\boldsymbol{\rho}_p^+ & , \boldsymbol{r} \in \Omega_p^+ \\ \\ \frac{A_{4p}}{3V_p^-}\boldsymbol{\rho}_p^- & , \boldsymbol{r} \in \Omega_p^- \end{cases} \tag{B.1}$$

where A_{4p} represents the area of the shared facet, $V_p^{\pm}$ are the volumes of $\Omega_p^{\pm}$, $\boldsymbol{\rho}_p^{\pm}$ are the position vectors with respect to tetrahedral vertices $O_p^{\pm}$, and $\boldsymbol{r}$ is the position vector with respect to the global origin O, as shown in Fig. B.1.

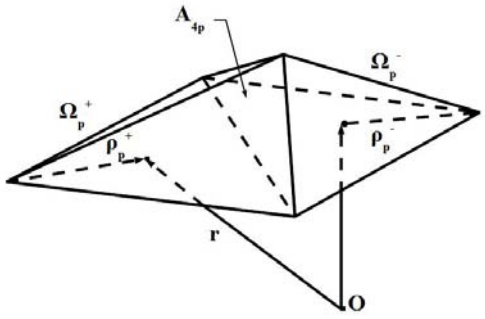

Figure B.1: Tetrahedron pair and geometrical parameters associated with the pth SWG basis function

The basis function $\boldsymbol{v}_p$ is used to approximately represent the surface current, and some of its properties are:

1. $\boldsymbol{v}_p$ has the normal component to any face equal to zero except for the shared facet of the tetrahedral pair $\Omega_p^{\pm}$, which is constant and continuous across the facet;

2. if the pth facet belongs to the boundary surface S_P of the plasma volume V_P, $\boldsymbol{v}_p$ may have support just on tetrahedron Ω_p^+, viz.,

$$\boldsymbol{v}_p(\boldsymbol{r}) = \begin{cases} \frac{A_{4p}}{3V_p^+}\boldsymbol{\rho}_p^+ & , \boldsymbol{r} \in \Omega_n^+ \\ 0, & \text{otherwise,} \end{cases} \tag{B.2}$$

   The latter type of functions is required to account for the physical fact that $\boldsymbol{D}_P \cdot \hat{\boldsymbol{n}}$ is nonzero on S_P;

3. the divergence in $\Omega_p^{\pm}$ of $\boldsymbol{v}_p$ is proportional to the charge density associated with the tetrahedral patch, and it is

$$\nabla \cdot \boldsymbol{v}_p(\boldsymbol{r}) = \pm \frac{1}{\left(\rho_n^{\pm}\right)^2} \frac{\delta\left(\rho_p^{\pm}\right)^2 v_p}{\delta \rho_p^{\pm}} = \begin{cases} \frac{A_{4p}}{V_p^+}, & \boldsymbol{r} \in \Omega_p^+ \\ -\frac{A_{4p}}{V_p^-}, & \boldsymbol{r} \in \Omega_p^- \\ 0, & \text{otherwise} \end{cases} \tag{B.3}$$

   We can conclude that the charge density is constant within each tetrahedron.

We can approximate the current distribution in the plasma volume in terms of the $\boldsymbol{v}_p$ as

$$\boldsymbol{D}_P \cong \sum_{P=1}^{N_P} \boldsymbol{v}_p(\boldsymbol{r})\, D_P, \tag{B.4}$$

where N_P is the number of tetrahedral facets.

Appendix C

System matrix and excitation vector

The entries of the MoM matrix result from the combination of at most four terms, e.g.,

$$(Z_{AA})_{mn} = \sum_{\alpha,\beta} (Z_{AA})_{mn}^{\alpha\beta}, \tag{C.1}$$

and corresponding expressions for the other sub-blocks.

The elementary contributions are

$$\begin{aligned}
&(Z_{AA})_{mn}^{\alpha\beta} = \\
&= -\mathrm{j}\, k_0 \int_{T_m^\alpha} \mathrm{d}^2 r \int_{T_n^\beta} \mathrm{d}^2 r' \mathbf{f}_m^\alpha(\mathbf{r}) \cdot \left(\bar{\mathbf{I}} - \frac{\nabla_\mathrm{s} \nabla'}{k_0^2} \right) G(R) \cdot \mathbf{f}_n^\beta(\mathbf{r}') \\
&= -\mathrm{j}\, k_0 \int_{T_m^\alpha} \mathrm{d}^2 r \int_{T_n^\beta} \mathrm{d}^2 r' G(R)\, \mathbf{f}_m^\alpha(\mathbf{r}) \cdot \mathbf{f}_n^\beta(\mathbf{r}') \\
&\quad - \frac{1}{\mathrm{j}\, k_0} \int_{T_m^\alpha} \mathrm{d}^2 r \int_{T_n^\beta} \mathrm{d}^2 r' G(R)\, (\nabla_\mathrm{s} \cdot \mathbf{f}_m^\alpha)(\nabla'_\mathrm{s} \cdot \mathbf{f}_n^\beta)
\end{aligned} \tag{C.2}$$

$$\begin{aligned}
&(Z_{PA})_{qn}^{\alpha\beta} = \\
&= \mathrm{j}\, k_0 \int_{\Omega_q^\alpha} \mathrm{d}^3 r \int_{T_n^\beta} \mathrm{d}^2 r' \boldsymbol{v}_q^\alpha(\mathbf{r}) \cdot \left(\bar{\mathbf{I}} - \frac{\nabla \nabla'}{k_0^2} \right) G(R) \cdot \mathbf{f}_n^\beta(\mathbf{r}') \\
&= \mathrm{j}\, k_0 \int_{\Omega_q^\alpha} \mathrm{d}^3 r \int_{T_n^\beta} \mathrm{d}^2 r' G(R)\, \boldsymbol{v}_q^\alpha(\mathbf{r}) \cdot \mathbf{f}_n^\beta(\mathbf{r}') \\
&\quad + \frac{1}{\mathrm{j}\, k_0} \int_{\Omega_q^\alpha} \mathrm{d}^3 r \int_{T_n^\beta} \mathrm{d}^2 r' G(R)\, (\nabla \cdot \boldsymbol{v}_q^\alpha)(\nabla'_\mathrm{s} \cdot \mathbf{f}_n^\beta) \\
&\quad - \frac{1}{\mathrm{j}\, k_0} \int_{\partial\Omega_{4q}^\alpha} \mathrm{d}^2 r \int_{T_n^\beta} \mathrm{d}^2 r' G(R)\, \hat{\mathbf{n}}_{4q}^\alpha \cdot \boldsymbol{v}_q^\alpha(\mathbf{r})\, (\nabla'_\mathrm{s} \cdot \mathbf{f}_n^\beta),
\end{aligned} \tag{C.3}$$

$$
\begin{aligned}
&(Z_{AP})_{mp}^{\alpha\beta} = \\
&\int_{T_m^\alpha} \mathrm{d}^2 r \int_{\Omega_p^\beta} \mathrm{d}^3 r' \mathbf{f}_m^\alpha(\mathbf{r}) \cdot \left(k_0^2 \overline{\mathbf{I}} - \nabla_\mathrm{s} \nabla'\right) G(R) \cdot [\overline{\boldsymbol{\alpha}}(\mathbf{r}') \cdot \boldsymbol{v}_p^\beta(\mathbf{r}')] \\
&= k_0^2 \int_{T_m^\alpha} \mathrm{d}^2 r \int_{\Omega_p^\beta} \mathrm{d}^3 r' G(R)\, \mathbf{f}_m^\alpha(\mathbf{r}) \cdot \overline{\boldsymbol{\alpha}}(\mathbf{r}_p'^\beta) \cdot \boldsymbol{v}_p^\beta(\mathbf{r}') \\
&\quad - \int_{T_m^\alpha} \mathrm{d}^2 r \int_{\Omega_p^\beta} \mathrm{d}^3 r' G(R) \left(\nabla_\mathrm{s} \cdot \mathbf{f}_m^\alpha\right) \nabla' \cdot [\overline{\boldsymbol{\alpha}}(\mathbf{r}_p'^\beta) \cdot \boldsymbol{v}_p^\beta] \\
&\quad + \int_{T_m^\alpha} \mathrm{d}^2 r \int_{\partial\Omega_p^\beta} \mathrm{d}^2 r' G(R) \left(\nabla_\mathrm{s} \cdot \mathbf{f}_m^\alpha\right) \hat{\mathbf{n}}_p'^\beta \cdot \overline{\boldsymbol{\alpha}}(\mathbf{r}_p'^\beta) \cdot \boldsymbol{v}_p^\beta(\mathbf{r}'),
\end{aligned} \tag{C.4}
$$

$$
\begin{aligned}
(Z_{PP})_{qp}^{\alpha\beta} &= \int_{\Omega_q^\alpha \cap \Omega_p^\beta} \mathrm{d}^3 r\ \boldsymbol{v}_q^\alpha \cdot \overline{\boldsymbol{\varepsilon}}_r^{-1} \cdot \boldsymbol{v}_p^\beta \\
&- \int_{\Omega_q^\alpha} \mathrm{d}^3 r \int_{\Omega_p^\beta} \mathrm{d}^3 r' \boldsymbol{v}_q^\alpha(\mathbf{r}) \cdot \left(k_0^2 \overline{\mathbf{I}} - \nabla\nabla'\right) G(R) \cdot [\overline{\boldsymbol{\alpha}}(\mathbf{r}') \cdot \boldsymbol{v}_p^\beta(\mathbf{r}')] \\
&= \int_{\Omega_q^\alpha \cap \Omega_p^\beta} \mathrm{d}^3 r\ \boldsymbol{v}_q^\alpha \cdot \overline{\boldsymbol{\varepsilon}}_r^{-1}(\mathbf{r}_q^\alpha) \cdot \boldsymbol{v}_p^\beta \\
&- k_0^2 \int_{\Omega_q^\alpha} \mathrm{d}^3 r \int_{\Omega_p^\beta} \mathrm{d}^3 r' G(R)\, \boldsymbol{v}_q^\alpha(\mathbf{r}) \cdot \overline{\boldsymbol{\alpha}}(\mathbf{r}_p'^\beta) \cdot \boldsymbol{v}_p^\beta(\mathbf{r}') \\
&+ \int_{\Omega_q^\alpha} \mathrm{d}^3 r \int_{\Omega_p^\beta} \mathrm{d}^3 r' G(R) \left(\nabla \cdot \boldsymbol{v}_q^\alpha\right) \nabla' \cdot [\overline{\boldsymbol{\alpha}}(\mathbf{r}_p'^\beta) \cdot \boldsymbol{v}_p^\beta] \\
&- \int_{\Omega_q^\alpha} \mathrm{d}^3 r \int_{\partial\Omega_p^\beta} \mathrm{d}^2 r' G(R) \left(\nabla \cdot \boldsymbol{v}_q^\alpha\right) \hat{\mathbf{n}}_p'^\beta \cdot \overline{\boldsymbol{\alpha}}(\mathbf{r}_p'^\beta) \cdot \boldsymbol{v}_p^\beta(\mathbf{r}') \\
&- \int_{\partial\Omega_{4q}^\alpha} \mathrm{d}^2 r \int_{\Omega_p^\beta} \mathrm{d}^3 r' G(R)\, \hat{\mathbf{n}}_{4q}^\alpha \cdot \boldsymbol{v}_q^\alpha(\mathbf{r})\, \nabla' \cdot [\overline{\boldsymbol{\alpha}}(\mathbf{r}_p'^\beta) \cdot \boldsymbol{v}_p^\beta] \\
&+ \int_{\partial\Omega_{4q}^\alpha} \mathrm{d}^2 r \int_{\partial\Omega_p^\beta} \mathrm{d}^2 r' G(R)\, \hat{\mathbf{n}}_{4q}^\alpha \cdot \boldsymbol{v}_q^\alpha(\mathbf{r})\ \hat{\mathbf{n}}_p'^\beta \cdot \overline{\boldsymbol{\alpha}}(\mathbf{r}_p'^\beta) \cdot \boldsymbol{v}_p^\beta(\mathbf{r}'),
\end{aligned} \tag{C.5}
$$

where $\mathbf{r}_q^\alpha$ ($\mathbf{r}_p'^\beta$) is the position vector of the center of Ω_q^α (Ω_p^β), $\hat{\mathbf{n}}_{4q}^\alpha$ ($\hat{\mathbf{n}}_p'^\beta$) represents the outward-pointing unit vector normal to the facet $\partial\Omega_{4q}^\alpha$ (the facets of Ω_p^β).

The surface and 3-D divergences appearing in the above formulas are computed as

$$
\nabla_\mathrm{s} \cdot \mathbf{f}_m^\alpha = s_\alpha \frac{l_{3m}}{A_m^\alpha}, \qquad \nabla_\mathrm{s}' \cdot \mathbf{f}_n^\beta = s_\beta \frac{l_{3n}}{A_n^\beta}, \tag{C.6a}
$$

$$
\nabla \cdot \boldsymbol{v}_q^\alpha = s_\alpha \frac{A_{4q}}{V_q^\alpha}, \tag{C.6b}
$$

$$
\nabla' \cdot [\overline{\boldsymbol{\alpha}}(\mathbf{r}_p'^\beta) \cdot \boldsymbol{v}_p^\beta] = s_\beta \,\mathrm{Tr}\, \overline{\boldsymbol{\alpha}}(\mathbf{r}_p'^\beta) \frac{A_{4p}}{3V_p^\beta}, \tag{C.6c}
$$

where $\mathrm{Tr}\, \overline{\boldsymbol{\alpha}}$ is the trace of $\overline{\boldsymbol{\alpha}}$, and $s_{\alpha,\beta} = \pm 1$ for $\alpha, \beta = \pm$.

The entries of the metal surface part of the excitation vector $[V_G]$ are non-zero only when the test function $\mathbf{f}_m$ is associated with the surface-mesh inner edges that model the port region. In such case, if we assume, e.g., $\hat{\boldsymbol{\nu}} = \hat{\boldsymbol{\nu}}_m^+$, the entries read

$$(V_G)_m = \int_{T_m^+ \cup T_m^-} \mathrm{d}^2 r\, \mathbf{f}_m \cdot \mathbf{E}_{AA}^{\mathrm{i}} = \int_{\partial T_{3m}^+} \mathrm{d}r\, \mathbf{f}_m^+ \cdot \hat{\boldsymbol{\nu}}_m^+ V_G = V_G l_{3m}, \tag{C.7}$$

where l_{3m} is the length of ∂T_{3m}^+ and we have used the normalization condition $\mathbf{f}_m^+ \cdot \hat{\boldsymbol{\nu}}_m^+ = 1$.

Bibliography

[1] I. Alexeff, T. Anderson *et al.*, "Experimental and theoretical results with plasma antennas," *IEEE Trans. on Antennas Propagation*, vol. 7, pp. 2198 – 2202, 2000.

[2] M. Hargreave, J. P. Rayner, A. Cheetam, G. N. French, and A. P. Whichello, "Coupling power and information to a plasma antenna," in *11th International Congress on Plasma Physics*, 2002.

[3] G. Cerri, R. D. Leo, V. M. Primiani, and P. Russo, "Measurement of the properties of a plasma column used as a radiating element," *IEEE Trans. on Instr. and Measurem*, vol. 57, no. 2, p. 242, 2008.

[4] A. Zhu, Z. Chen, J. Lv, and J. Liu, "Characteristics of a DC-Biased Plasma Antenna and plasma antenna excited by surface wave," *Journ. Electromagnetic Analysis and Applications*, p. 280, 2012.

[5] T. Anderson, *Plasma Antennas*, A. House, Ed., 2011.

[6] L. Wei, Q. Jinghui, and S. Ying, "Analysis and design of plasma monopole antenna," in *International Conference on Antenna Theory and Techniques*, 2009, pp. 200–202.

[7] W. L. Kang, M. Rades, and I. Alexeff, "A conceptual study of stealth plasma antenna," in *IEEE International Conference on Plasma Science*, 1996.

[8] W. M. Manheimer, "Plasma reflectors for electronic beam steering on radar system," *IEEE Trans. on Plasma Science*, vol. 19, 1991.

[9] A. E. Robson, R. L. Morgan, and R. A. Meger, "Demonstration of a plasma mirror for microwaves," *IEEE Trans. on Plasma Science*, vol. 20, pp. 1036– 1040, 1992.

[10] J. Mathew, R. A. Meger, J. A. Gregor, R. E. Pechacek, R. F. Fensler, and W. M. Manheimer, "Electronically steerable plasma mirror for radar applications," in *IEEE International Radar Conference*, 1995.

[11] T. Anderson and I. Alexeff, "Theory and experiments of plasma antenna radiation emitted through plasma apertures or windows with suppressed back and side lobes," in *29th IEEE International Conference on Plasma Science*, 2002.

[12] D. C. Jenn and W. V. T. Rusch, "Low-sidelobe reflector synthesis and design using resistive surfaces," *IEEE Trans. on Antennas and Propagation*, vol. 39, pp. 1372 – 1375, 1991.

[13] W. M. Manheimer, "Fast, high power microwave components based on beam generated plasmas," US Naval Research Laboratory, Tech. Rep., 1998.

[14] N. P. Stogniy and N. K. Sakhnenko, "Coupled plasma cylindrical columns as subwavelength antenna," *VIII International Conference on Antenna Theory and Techniques*, 2011.

[15] X. P. Wu, J. M. Shi, Z. S. Chen, and B. Xu, "A new plasma antenna of beam forming," *Progress In Electromagnetics Research*, vol. 126, pp. 539–553, 2012.

[16] F. Sadeghikia and F. Hodjat-Kashani, "A two element plasma antenna array," *Engineering, Technology and Applied Science Research*, vol. 5, pp. 516–521, 2013.

[17] Z. Dai, S. Liu, Y. Chen, and N. Gao, "Development and investigation of reconfigurable plasma antennas," *IEEE Microwave and Millimeter Wave Technology International Conference*, vol. 1, pp. 1135–1137, 2010.

[18] T. Anderson *et al.*, "An operating intelligent plasma antenna," *IEEE16th International Pulsed Power Conference*, vol. 1, pp. 353–356, 2007.

[19] R. J. Mailloux, *Phased Array Antenna Handbook*, B. Artech House, Ed., 1994.

[20] M. Moisan and Z. Zakrzewski, "Plasma sources based on the propagation of electromagnetic surface waves," *J. Phys. D, Appl. Phys.*, vol. 24, pp. 1025–1048, 1991.

[21] M. Lieberman and A. Lichtenberg, *Principles of Plasma Discharges and Material Processing*, J. W. New York, Ed., 1994.

[22] J. P. Rayner, A. P. Whichello, and A. D. Cheetham, "Physical characteristics of plasma antennas," *IEEE Transactions on Plasma Science*, vol. 32, pp. 269–281, 2004.

[23] P. Russo, G. Cerri, and E. Vecchioni, "Self-consistent model for the characterization of plasma ignition by propagation of an electromagnetic wave to be used for plasma antennas design," *IET Microwaves, Antennas and Propagation*, vol. 4, pp. 2256–2264, 2010.

[24] ——, "Self-consistent analysis of cylindrical plasma antennas," *IEEE Trans. on Antennas and Propagation*, vol. 59, p. 1503, 2011.

[25] Y. Lee and S. Ganguly, "Analysis of a plasma-column antenna using FDTD method," *Microw. Opt. Technol. Lett.*, vol. 46, pp. 252–259, 2005.

[26] X. Li, F. Luo, and B. Hu, "FDTD analysis of radiation performance of a cylinder plasma antenna," *IEEE Antennas Wireless Propag. Lett.*, vol. 8, pp. 756–758, 2009.

[27] F. Sadeghikia, F. Hodjat-Kashani, and R.-M. J., "Characterization of a surface wave driven plasma monopole antenna," *Journal of Electromagnetic Waves and Apllications*, vol. 26, pp. 239–250, 20012.

[28] D. Melazzi *et al.*, "ADAMANT: A surface and volume integral-equation solver for the analysis and design of helicon plasma sources," *Computer Physics Communication*, 2014, in press.

[29] J. Hettinger, "Aerial conductor for wireless signaling and other purposes," US Patent 1 309 031, 1919.

[30] T. Anderson *et al.*, "Antenna having reconfigurable length," US Patent 6 710 746 B1, 2004.

[31] Norris *et al.*, "Reconfigurable plasma antenna," US Patent 6 369 763 B1, 2002.

[32] T. Anderson *et al.*, "Multiple tube plasma antenna," US Patent 5 693 169, 1999.

[33] T. J. Pavliscak *et al.*, "Gas plasma antenna," US Patent 7 474 273 B1, 2009.

[34] T. Anderson, "Configurable arrays for steerable antennas and wireless network incorporating the steerable antennas," US Patent 6 870 517 B1, 2005.

[35] X. S. Li and B. J. Hu, "FDTD analysis of a magneto-plasma antenna with uniform or nonuniform distribution," *IEEE Antennas and Wireless Propagation Letters*, vol. 9, 2010.

[36] R. Harrington, *Field Computation by Moment Methods*, M. New York, Ed., 1968.

[37] S. Rao, D. Wilton, and A. Glisson, "Electromagnetic scattering by surfaces of arbitrary shape," *IEEE Trans. on Antennas and Propagation*, vol. 30, pp. 409–418, 1982.

[38] D. H. Schaubert, D. R. Wilton, and A. W. Glisson, "A tetrahedral modeling method for electromagnetic scattering by arbitrarily shaped inhomogeneous dielectric bodies," *IEEE Transactions on Antennas and Propagation*, vol. 32, pp. 77–85, 1984.

[39] C. Geuzaine and J. F. Remacle. Gmsh: a three-dimensional finite element mesh generator with built-in pre- and post-processing facilities.